Contents lists available at ScienceDirect

# Journal of Alloys and Compounds

journal homepage: http://www.elsevier.com/locate/jalcom



# Mechanical, corrosion, and wear properties of biomedical Ti–Zr–Nb–Ta–Mo high entropy alloys



Nengbin Hua <sup>a, \*</sup>, Wenjie Wang <sup>a</sup>, Qianting Wang <sup>a</sup>, Youxiong Ye <sup>b</sup>, Sihan Lin <sup>a</sup>, Lei Zhang <sup>a</sup>, Oiaohang Guo <sup>a</sup>, Jamieson Brechtl <sup>c</sup>. Peter K. Liaw <sup>b</sup>

- <sup>a</sup> Department of Materials Science and Engineering, Fujian Provincial Key Laboratory of Advanced Materials Processing and Application, Fujian University of Technology, 350118, Fuzhou, China
- <sup>b</sup> Department of Materials Science and Engineering, The University of Tennessee, 37996, 2200 Knoxville, TN, USA
- <sup>c</sup> The Bredesen Center for Interdisciplinary Research and Graduate Education, The University of Tennessee, 37996, 3394 Knoxville, TN, USA

#### ARTICLE INFO

Article history:
Received 27 August 2020
Received in revised form
15 November 2020
Accepted 16 November 2020
Available online 21 November 2020

Keywords:
High entropy alloys
Wear
Corrosive wear
Polarization
Mechanical properties

#### ABSTRACT

The microstructures, mechanical, corrosion, and wear behaviors of the  $Ti_xZrNbTaMo~(x=0.5,1,1.5,$  and 2, molar ratio) high entropy alloys (HEAs) were studied. It was found that the Ti-Zr-Nb-Ta-Mo~HEAs showed a dendrite structure with two body-centered-cubic (BCC) solid solution phases. The  $Ti_{0.5}ZrNb-TaMo~HEA$  exhibited a high hardness of about 500 HV, high compressive strength approaching 2,600 MPa, and large plastic strain of over 30%. Furthermore, the highly-protective oxide films formed on the surface of Ti-Zr-Nb-Ta-Mo~HEAs in the phosphate buffer saline (PBS) solution, which resulted in the high corrosion resistance of the HEAs. The Ti-Zr-Nb-Ta-Mo~HEAs exhibited the greater dry- and wet-wear resistance than that of the traditional biomedical Ti6Al4V alloy. The results also indicated that with the decrease in the Ti content, the wear resistance of the Ti-Zr-Nb-Ta-Mo~HEAs in the PBS solution improved. Finally, the  $Ti_{0.5}ZrNbTaMo~alloy~presented$  the highest corrosive wear resistance among the four HEAs owing to its combination of good mechanical properties and high chemical stability.

© 2020 Elsevier B.V. All rights reserved.

# 1. Introduction

Biomedical implant materials are widely used to repair or replace damaged biological tissues. Compared with ceramics and polymers, metals exhibit significant advantages as biomedical implant materials due to their high strength and plasticity. To date, applications of biomedical metallic materials, consisting of the Ti and Ti-based alloys, 316L stainless steels, CoCrMo alloys, NiTi alloys, include artificial hip joints, cardiovascular stents, bone plates, dental implants, and surgical instruments [1,2]. Among these conventional biomedical materials, Ti-based alloys have become the first choice for orthopedic and dental implant products since they exhibit the good biocompatibility and mechanical properties, high corrosion resistance, and relatively-low Young's modulus [3]. However, the Ti-based alloys usually suffer from an unsatisfactory wear property. As implant materials working in the physiological environment, the Ti-based alloy can be significantly affected by the

E-mail address: flower1982cn@126.com (N. Hua).

corrosion wear failure and "particle disease" caused by wear debris [4,5]. Moreover, biomedical Ti-based amorphous alloys display higher strength and hardness as compared to crystalline Ti-based alloys, which gives them superior wear resistance under dry friction. Nevertheless, Ti-based amorphous alloys are very susceptible to pitting corrosion that generally occurs in physiological solutions, and, can significantly accelerate their wear degradation during the tribocorrosion process. Meanwhile, the size limitation and low plasticity of Ti-based amorphous alloys restrict their clinical application as implant materials [6–10]. Therefore, the development of new biomedical implant alloys with the high corrosion and wear resistance has been the focus of recent biomedical material investigations.

High entropy alloys (HEAs) are advanced metallic materials that have been developed over the past decade and are characterized as a multi-element solid solution structure alloy. Furthermore, HEAs are composed of a variety of elements mixed in an equimolar or nearly equimolar ratio [11–14]. The high configurational entropy effect, lattice distortion effect, and sluggish diffusion effect in HEAs give them their desirable mechanical properties as well as a stable structure [11–14]. Based on the multi-principal component design

 $<sup>\</sup>ast$  Corresponding author. School of Materials Science and Engineering, Fujian University of Technology, Fuzhou 350118, China.

concept, many HEA systems, including transition metal (Fe, Co, Cr, Ni, Mn, etc.) systems [12–16], Al-transition metal systems [17–19], and refractory metal (Ti, Zr, Nb, Ta, Hf, W, Mo,V, etc.) systems have been developed [20–28]. Such a variety of different HEA systems can, therefore, offers a wide range of options in terms of developing novel structural and functional metallic materials. So far, it has been reported that the Ti–Zr-based refractory HEAs [20–29] have excellent physical, chemical, and biological properties, and show promising potential in the field of biomedical implant materials.

Compared with traditional biomedical alloys, Ti-Zr-based refractory HEAs possess several advantages as orthopedic implant materials. Owing to the body-centered-cubic (BCC) solid solution structure, the Ti-Zr-based refractory HEAs usually exhibit the high hardness and good wear resistance, which can decrease the effect of "wear debris diseases" [30-32]. Although the conventional biomedical titanium alloys (such as Ti6Al4V) have good biocompatibility, they are not suitable as a bearing support surface because of the poor wear resistance resulting from the low shear strength of the surface oxide layer [3,4]. The CoCrMo alloy has excellent wear resistance and is often used as the supporting surface of artificial joint prosthesis. However, in recent years, it was found that for the patients implanted with the CoCrMo alloy, cobalt and chromium may have been released into the blood stream, possibly causing deleterious effects in the body [5]. For example, many biocompatibility studies have shown that the metal particles produced during wear may be related to cytotoxicity, DNA damage, metal allergy, and the presence of tumors [5].

Besides the high wear resistance, the high specific strength of the Ti–Zr-based refractory HEAs enables implanted devices, such as bone screws, to withstand thinner screw rods and deeper threads while resisting the plastic deformation and fracture under an applied stress [20,21,23,27,28]. Moreover, the Ti, Nb, Ta, Mo, Zr, and Hf elements have been reported to exhibit good corrosion resistance in simulated human fluids, and thus can form a highlyprotective surface film on the alloys. Here, the dense oxide film can hinder the dissolution of metal ions and reduce the negative effects of corrosion products on the acceptor [33–35]. Furthermore, from the perspective of biological safety, the alloy components of the Ti-Zr-based refractory HEAs do not contain highly-biotoxic elements, such as Ni, Al, Co, and Cu. The results of in vitro cell experiments show that the surface of the Ti-Zr-based refractory HEAs can support normal cell attachment and spreading, and the number of adherent cells is significantly higher than that of pure Ti, indicating their good biocompatibility [24–26]. In summary, the Ti–Zrbased refractory HEAs, which possess good comprehensive properties, are potentially viable candidates in the application of fracture internal fixation screws, artificial hip joints, dental materials, and medical stents.

Orthopedic implant materials inevitably undergo friction and wear with surrounding tissues while they are in operation in the human body. Meanwhile, due to the corrosive environment in the human body, the wear is often accompanied by corrosion, which results in corrosive wear [36,37]. The amount of material loss due to the corrosive wear is often greater than that separately caused by the corrosion and wear. Therefore, implant alloys should possess both high corrosion and wear resistance in the physiological environment. Interactions between corrosion and wear in the simulated physiological environment have been observed for traditional biomedical metallic materials, such as the Ti-based and Co-Cr-Mo alloys, as well as 316L stainless steel [38-41]. As potential biomedical implant materials, the corrosive wear behavior is one of the factors that can affect the long-term service reliability of the Ti-Zr-based refractory HEAs. Furthermore, the multi-principal component characteristics of the HEAs, which are different from the traditional alloy, may affect the corrosive wear behavior and

mechanism over time. However, the corrosive wear behavior and mechanism of HEAs in the simulated physiological environment are still not well understood.

It was found that adjusting the content of constituent elements in HEAs could affect their microstructure, corrosion, and wear behaviors [33,34]. The as-cast Ti–Zr-based refractory HEAs generally form a dendrite structure consisting of mainly BCC solid solution phases, which gives them their high hardness and wear resistance [27–32]. By adjusting the ratio of constituent elements of the Ti–Nb–Ta–Zr and Ti–Nb–Ta–Zr–Mo alloys, the dendrite morphology and the mechanical properties can be manipulated. Furthermore, it is worth noting that Nb, Ta, Mo, and other easily-passivated elements usually improve the chemical stability of the oxide film on the alloy surface [33–35]. Therefore, it is of great significance to study the influence of the contents of constituent elements on the microstructures, corrosion, and wear behaviors of the Ti–Zr refractory HEA system.

#### 2. Experimental

# 2.1. Sample preparation and structure characterization

The Ti, Nb, Ta, Zr, and Mo raw materials with a purity of more than 99.5 wt percent (wt.%) were used to prepare HEAs with the nominal composition of  $Ti_xZrNbTaMo$  (x = 0.5, 1, 1.5, and 2, molar ratio). The master alloy ingot was arc melted and cooled on a watercooled copper crucible in a high-purity argon protective atmosphere for at least 5 times to ensure the chemical homogeneity. Wire cut electrical discharge machining (WEDM) was used to fabricate bar-  $(2 \times 2 \times 4 \text{ mm}^3)$  and plate-  $(10 \times 10 \times 2 \text{ mm}^3)$  shape samples from the core region of the master alloy ingot. The surface of the alloy sample was ground with the silicon carbide sandpaper up to 2000 grit. The structure of the alloy sample was characterized via a Bruker-AXS-D8 X-ray diffractometer (XRD) and a JEOL JEM-1200EX transmission electron microscope (TEM). The structure and morphology of the samples were examined using a FEI-NovaNano450 scanning electron microscope (SEM). The chemical composition of the HEAs was determined by the energy dispersive X-ray spectroscopy (EDS).

# 2.2. Mechanical property tests

The microhardness test was carried out on a THVP-10 Vickers hardness tester using an applied load of 300 gf and a dwell time of 10 s. A DNS300 type mechanical testing system (MTS) was employed to record the room-temperature compression stress and strain curves of HEA samples. The compressive strain rate was set as  $2.1 \times 10^{-4} \, \mathrm{s}^{-1}$  and the sample gauge was  $2 \times 2 \times 4 \, \mathrm{mm}^3$ . After the compression test, the lateral surface morphologies of the compressed specimens were examined by SEM.

# 2.3. Wear behavior test

The reciprocating wear behaviors of the HEAs were tested by a HSR-2M tribology tester, using a Si<sub>3</sub>N<sub>4</sub> ball (6 mm in diameter) as the couple-pair. In the present study, the parameters of the wear experiment are as follows: a normal load of 5 N, an experiment time of 30 min, a sliding velocity of 60 r/min., and a friction reciprocating motion amplitude of 5 mm. During the sliding process, the coefficient of friction for the alloy samples was recorded. After the wear test, the wear volume ( $\Delta W$ ) of the alloy samples was determined by a MT-500 Probe-type material surface profile measuring instrument. The morphologies and compositions of the wear scars for the HEAs were examined by SEM and EDS, respectively.

#### 2.4. Corrosion behavior test

The three-electrode-cell system was used to access the corrosion behavior of the HEAs by an electrochemical workstation. For the experiment, the working electrode corresponded to the HEA samples while the counter electrode consists of a platinum plate. The saturated calomel electrode (SCE) was employed as the reference electrode. The potentiodynamic polarization curves of the HEAs were examined in the phosphate buffered saline (PBS) solution. The chemical compositions of the PBS solution were KCl: 0.20 g/L, NaCl: 8.01 g/L, KH<sub>2</sub>PO<sub>4</sub>: 0.20 g/L, Na<sub>2</sub>HPO<sub>4</sub>: 1.15 g/L and the pH value was between 7.4 and 7.46. Prior to the corrosion experiments, the surface of the alloy sample was polished with 2000 grit silicon carbide sandpapers. The as-polished specimens were ultrasonically cleaned in the acetone, ethanol, and deionized water. Before the potentiodynamic polarization test, the alloy sample was immersed in the PBS solution until the open circuit potential (OCP) reaches a stable state. After the polarization experiment, the corroded morphologies on the sample surface were examined by SEM, and the composition of the corroded surface was determined by EDS.

# 2.5. Surface chemistry

The compositions of the surface passive film for the HEAs, after immersion in the PBS solution for 24 h, were analyzed by an ESCALab250Xi X-ray photoelectron spectrometer (XPS). The full spectra for the HEAs and the Ti 2p, Zr 3d, Nb 3d, Ta 4f, Mo 3d, and O 1s narrow scan spectra were studied.

#### 3. Results

#### 3.1. Structure characterization of the Ti-Zr-Nb-Ta-Mo HEAs

Fig. 1 shows the XRD patterns of the as-cast  $Ti_xZrNbTaMo$  (x = 0.5, 1, 1.5, and 2) HEAs. It can be seen that the Ti-Zr-Nb-Ta-Mo HEAs exhibit sharp diffraction peaks, which

indicate that the structure is composed of two body-centered cubic (BCC) solid solution phase (labeled as BBC-1 and BBC-2 phases, respectively). The XRD patterns confirm the BCC structure of the HEAs without any intermetallic compound phase or ordered phase. With the decrease in the fraction of Ti in the alloys, the peak position of the minor BBC-2 phase shifts to lower angles. This shift to lower angles was accompanied by a decrease in the ratio of the peak intensity of the BBC-2 to the BBC-1 phase.

Fig. 2 displays the SEM morphologies of the (a) Ti<sub>0.5</sub>ZrNbTaMo, (b) TiZrNbTaMo, (c) Ti<sub>1.5</sub>ZrNbTaMo, and (d) Ti<sub>2</sub>ZrNbTaMo HEAs and the corresponding EDS mapping images of constituent elements consisting of the Ti, Zr, Nb, Ta, and Mo. The constituent elements on the surface of the TiZrNbTaMo HEA are presented on the EDS mapping images in Fig. 3. As can be seen, the microstructures of all the alloys are composed of the dendrite and the inter-dendrite matrix which are represented, respectively, by the regions of light gray and dark gray contrast. It was also determined that with a change in the Ti content, the microstructure of the HEAs changes. In Fig. 2(b), the TiZrNbTaMo alloy exhibits an equi-axis fine dendrite structure, which is consistent with previous reports on refractory HEAs [23-25]. A dendrite structure indicates the redistribution of the constituent elements during solidification. As seen in Fig. 3, Ta and Mo elements are enriched in the dendritic arms (light gray contrast), whereas the Ti, Zr, and Nb elements are enriched in the inter-dendrite matrix regions that are characterized by the dark gray contrast in the SEM image. The distribution of the constituent elements during solidification leads to the formation of the dendrite structure. The distribution of the constituent elements in the TiNbTaZrMo HEA can be qualitatively explained in terms of heat of mixing. During the solidification, the main-dendrite phase with high-melting-temperature elements, Ta (2996 °C) and Mo (2610 °C), was formed. In contrast, Ti and Zr were ejected from the dendrite phase because of the positive values of Ta, Nb, Ti, and Zr [23], resulting in the enrichment of the inter-dendrite region with relatively-low-melting-point elements: Ti (1668 °C) and Zr (1852 °C).

The decrease in the Ti corresponds to the relatively increase in

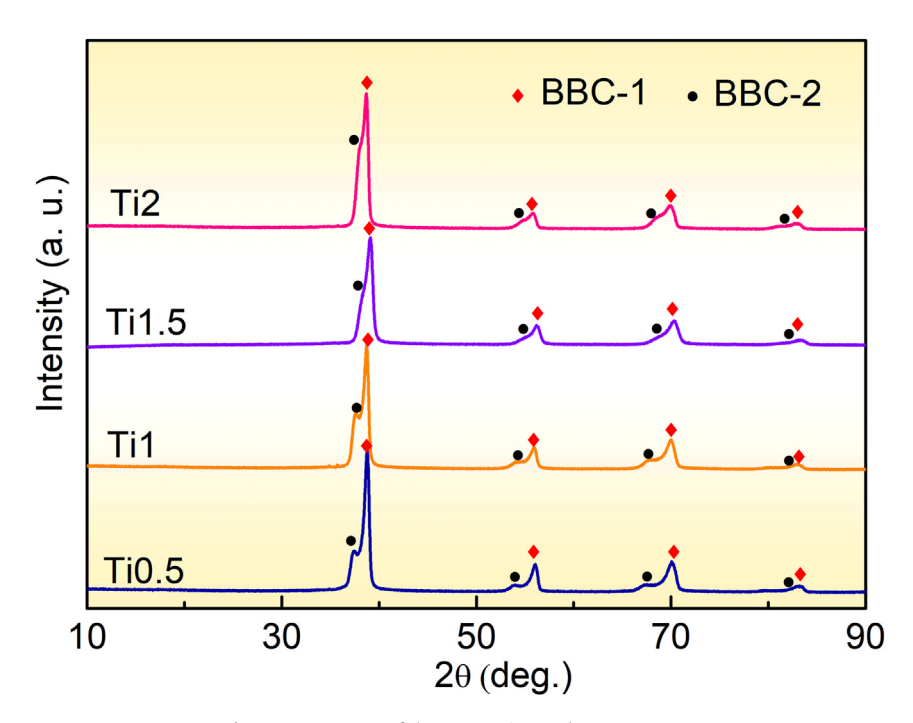


Fig. 1. XRD patterns of the as-cast Ti—Zr—Nb—Ta—Mo HEAs.

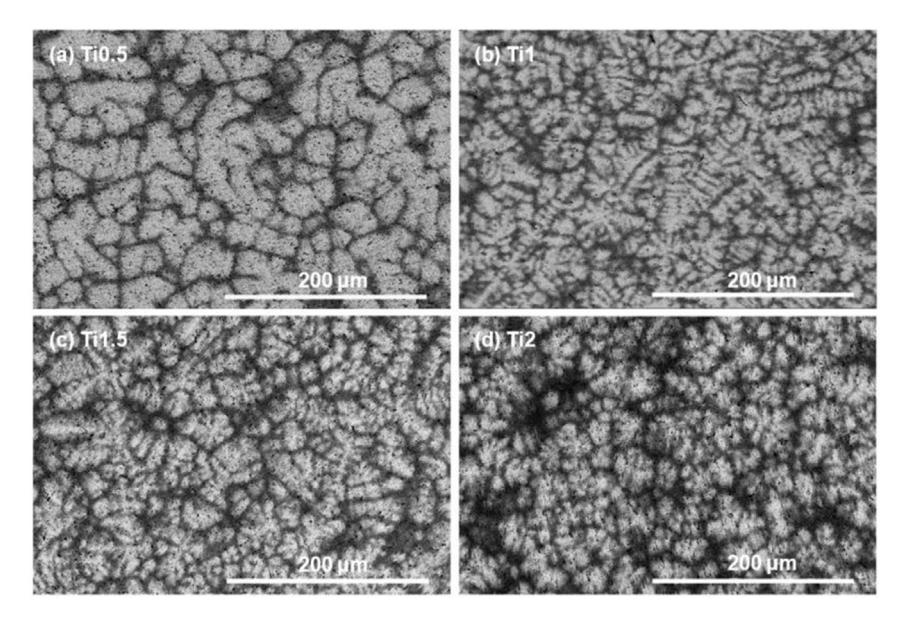


Fig. 2. SEM morphologies of the (a) Ti<sub>0.5</sub>ZrNbTaMo, (b) TiZrNbTaMo, (c) Ti<sub>1.5</sub>ZrNbTaMo, and (d) Ti<sub>2</sub>ZrNbTaMo HEAs.

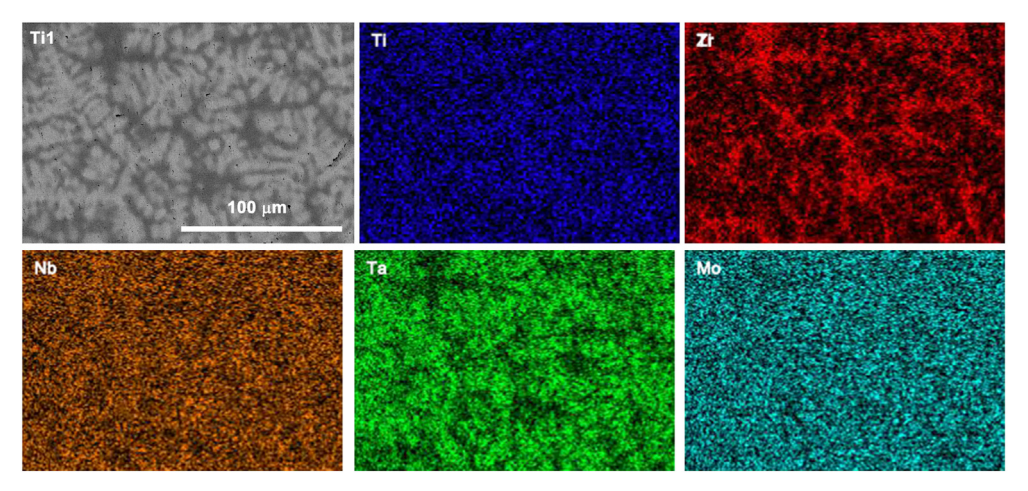


Fig. 3. SEM morphologies and the corresponding EDS mapping images of the TiZrNbTaMo HEA.

the fraction of high-melting-temperature elements Ta and Mo. During the solidification, more Ta and Mo present in the maindendrite phase leads to a noticeable coarsening of the dendrite arms, as can be observed in the  $\rm Ti_{0.5}ZrNbTaMo$  HEA from Fig. 2(a). On the other hand, an increase in Ti in the alloy composition results in the formation of short and round dendrite arms because of the increasing fraction of the low-melting-temperature element, as apparent in the SEM images for the  $\rm Ti_{1.5}ZrNbTaMo$  and  $\rm Ti_2ZrNbTaMo$  HEAS [see Fig. 2 (c)—(d)].

Fig. 4 presents the TEM bright-field images [(a) and (b)] as well as the corresponding selected area electron diffraction (SAED) patterns (insets) of the  $Ti_{0.5}ZrNbTaMo$  and  $Ti_2ZrNbTaMo$  HEAs, respectively. As apparent in the figure, no crystal precipitates from the BCC phases can be observed on the TEM images for both alloys [Fig. 4(a) and (b)]. Furthermore, the SAED patterns indicate that there is no ordered phase, such as the  $\omega$  phase or B2 structure, formed in the alloys during the solidification process [insets of Fig. 4(a) and (b)]. These results, therefore, verified that the BCC solid solution structure of the Ti-Zr-Nb-Ta-Mo HEAs that does not contain an obvious chemical order. During the solidification process, the distribution of constituent elements results in the

formation of the dendrite structure. The structure contains both the Ta-enriched main solid solution phase dendrite (BCC-1) as well as the Ti-, Zr-, and Nb-enriched minor solid solution phase (BCC-2) inter-dendrite matrix. During the solidification process, the main dendrite phase is formed by the high melting temperature elements Ta and Mo in the Ti–Zr–Nb–Ta–Mo HEAs. Because of the positive heat of mixing between Ta, Nb, Ti, and Zr, the Ti and Zr elements are first separated from the main dendrite phase and then enrich in the dendrite region.

Fig. 5 exhibits the compression stress-strain curves of the  $\rm Ti_2ZrNbTaMo~(x=0.5,1,1.5,$  and 2) HEAs at room temperature. As the Ti content increases, the yield strength of the Ti–Zr–Nb–Ta–Mo HEAs gradually decreases from 1,580 MPa for the Ti $_0.5$ ZrNbTaMo alloy to 1,440 MPa for the Ti $_2$ ZrNbTaMo alloy. However, the plastic deformation of the Ti–Zr–Nb–Ta–Mo HEAs decreases from 30% for the Ti $_0.5$ ZrNbTaMo alloy to 14% for the TiZrNbTaMo alloy and then increase to 30% for the Ti $_2$ ZrNbTaMo alloy. It is obvious that the Ti $_0.5$ ZrNbTaMo and Ti $_2$ ZrNbTaMo alloys exhibit the superior plastic deformation behavior among the four HEAs. It is also apparent from the compressive test results that the strength of the HEAs is correlated with their chemical composition

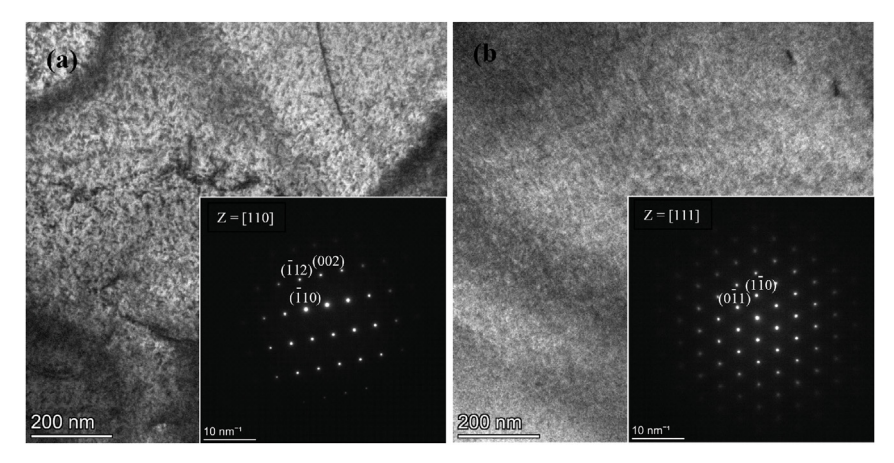


Fig. 4. TEM bright-field images [(a) and (b)] as well as corresponding selected area electron diffraction (SAED) patterns (insets) of the Ti<sub>0.5</sub>ZrNbTaMo and Ti<sub>2</sub>ZrNbTaMo HEAs, respectively.

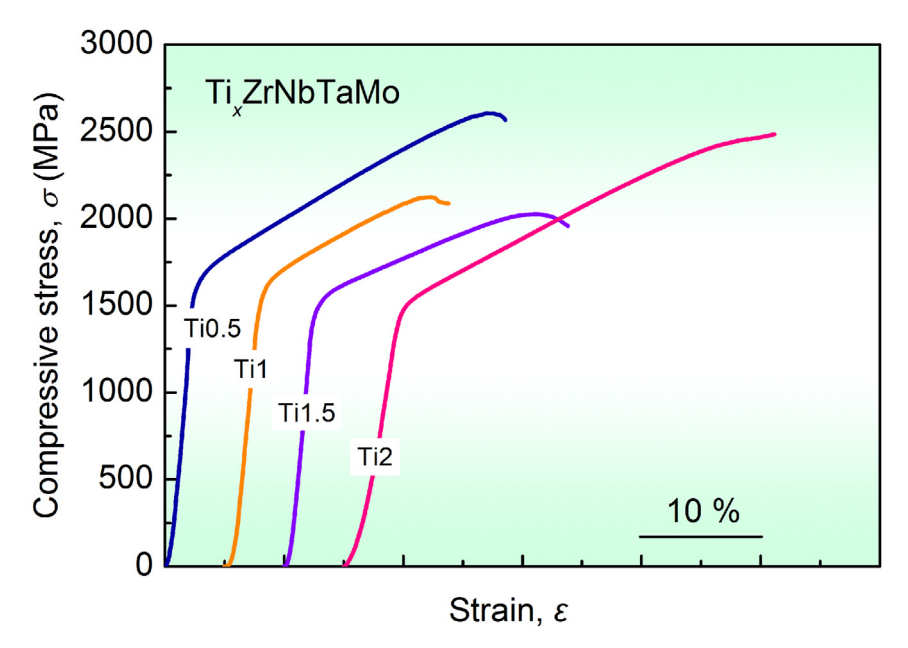


Fig. 5. Compression stress-strain curves of the  $Ti_xZrNbTaMo~(x=0.5,1,1.5,and~2)$  HEAs at room temperature.

and can be improved by reducing the Ti content of the alloys. With reducing Ti content, the relative fraction of the Ta and Mo in the HEA increases, which leads to an increasing amount of maindendrite phase enriching in Ta and Mo. Since the Young's modulus of Ta (186 GPa) and Mo (329 GPa) are much greater than those of the Ti (116 GPa), Zr (88 GPa), and Nb (105 GPa), the Young's modulus of low-Ti-fraction HEA is higher than those of high-Tifraction HEAs according to the rule of mixtures [25]. It was also found that the solid-solution strengthening Ti-Zr-Nb-Ta-Mo and Ti-Zr-Hf-Nb-Ta HEAs is primarily caused by the modulus misfit between atoms, and the Ta-Mo-enriched HEA possesses a larger modulus misfits and higher strength [25]. Therefore, with the increasing Ti content, the Ti-Zr-Nb-Ta-Mo HEAs exhibit a decreasing Young's modulus and thus the strength.

Furthermore, the plastic deformation capability of the HEAs is affected by their microstructures. For instance, the TiZrNbTaMo alloy that has a fine dendrite structure displays low plastic deformation. In contrast, the  $\rm Ti_{0.5}ZrNbTaMo$  alloy, which contains a coarsened dendrite structure, exhibits relatively greater plastic deformation that is accompanied by a high compressive strength

approaching 2.600 MPa. Meanwhile, the enhanced plasticity of the Ti<sub>0.5</sub>ZrNbTaMo HEA may be attributed to the discontinuous granular dendrite structure of the alloy. It is seen from Fig. 2 that the TiZrNbTaMo alloy shows an equi-axis fine dendrite structure, which is consistent with previous reports on refractory HEAs [23–25]. With decreasing Ti, the Ti<sub>0.5</sub>ZrNbTaMo HEA contains the dendritic phase with a well-developed dendritic morphology with coarse arms, which are almost linked up. The linked-up coarse dendritic structure usually corresponds to a larger plasticity than that with a equi-axis fine dendrite structure [42,43]. It was found that the annealed TiZrNbTaMo HEA sample display a greater plasticity than that of the as cast TiZrNbTaMo alloy [42]. The annealed TiZrNbTaMo HEA possess a coarsened dendrite structure which is identical with that of the Ti<sub>0.5</sub>ZrNbTaMo HEA [42]. Therefore, in this study, a drop in plasticity is observed by the compressive stress and strain curves for the TiZrNbTaMo, and Ti<sub>1.5</sub>ZrNbTaMo HEAs as compared to the Ti0.5ZrNbTaMo HEA owing to the change in the microstructural morphologies from a coarsened dendrite structure to an equi-axis fine dendrite structure. As the Ti content increases, the dendritic arms become much shorter. The Ti<sub>2</sub>ZrNbTaMo HEA

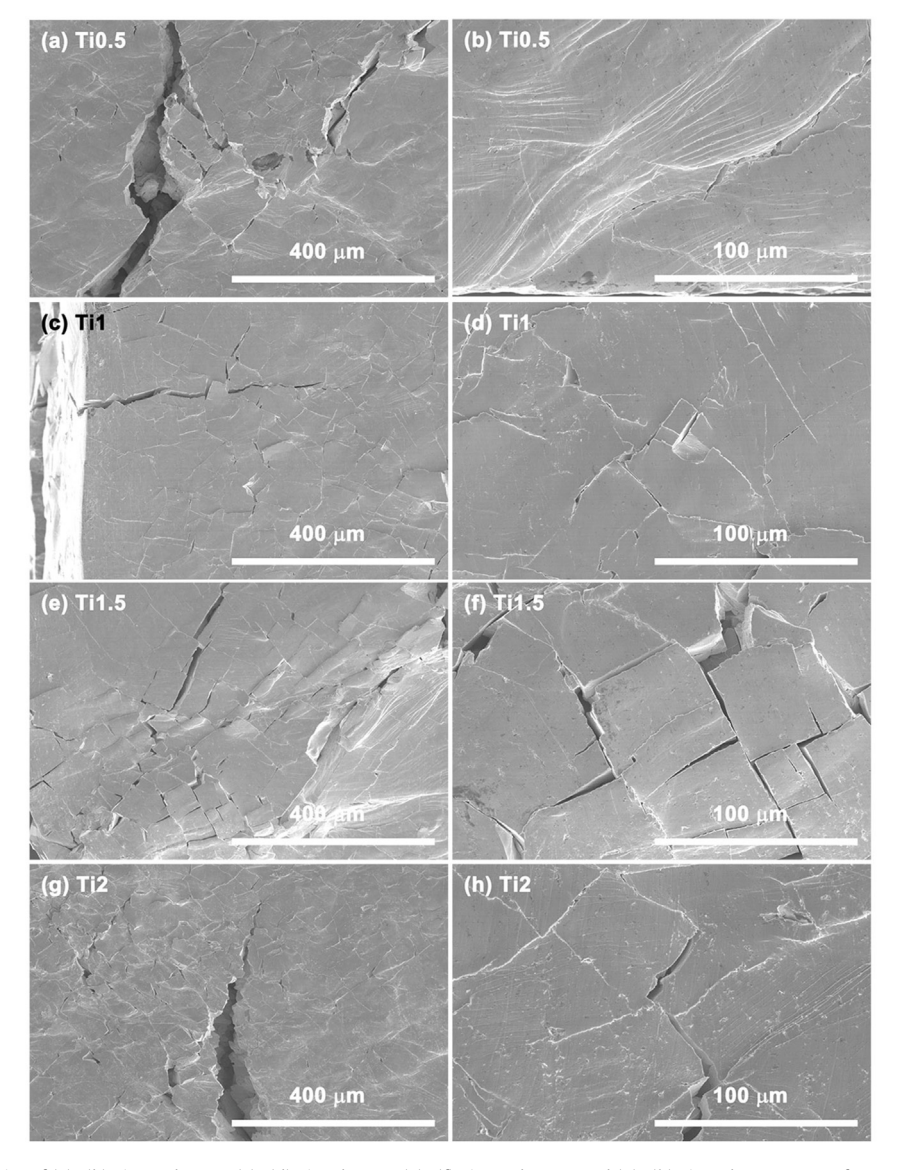
exhibits a dendrite structure with short and spherical arms, as seen in Fig. 2(d). It has been reported that the  $Ti_{60}Cu_{14}Ni_{12}Sn_4Nb_{10}$  alloy, which possessed a rounded dendrite with a few micrometers in length, showed the good compressive and tensile plasticity [44]. Compared with the equi-axis fine dendrite, the spherical dendrite shows a relatively smaller damage and splitting effect on the matrix, which can reduce the stress concentration and result in the enhanced plasticity [44]. Thus, as the Ti content increases, the  $Ti_2ZrNbTaMo$  HEA displays a larger compression strain, as revealed in Fig. 5.

Fig. 6 presents the SEM morphologies of the [(a) - (b)]  $Ti_{0.5}ZrNbTaMo, [(c) - (d)]$   $Ti_{2.5}ZrNbTaMo, [(c) - (f)]$   $Ti_{1.5}ZrNbTaMo, and [(g) - (h)]$   $Ti_{2.5}ZrNbTaMo$  HEAs after compression deformation. There are network-like micro- and macro-cracks on the surface of the compressively-deformed HEA samples, for which the number of cracks on the surface of the  $Ti_{0.5}ZrNbTaMo$  alloy are the least. Moreover, a large number of densely-distributed shear bands can be seen on the lateral surface of the  $Ti_{0.5}ZrNbTaMo$  alloy, which corresponds to the good plastic deformation ability. Furthermore, the surface of the TiZrNbTaMo and  $Ti_{1.5}ZrNbTaMo$  alloys display a

large number of network-like cracks in which the surface between the cracks is rather smooth with very few shear bands. This result indicates that local shear deformation occurred during the compression.

As the compression progresses, the highly-localized shear deformation induces the initiation and fast propagation of cracks along some main shear bands, leading to the rupture of HEAs. It is clear from Fig. 6(g) and (h) that although there are many network-like cracks present on the surface of the  $Ti_2ZrNbTaMo$  alloy, the shear bands caused by plastic deformation are readily apparent on the cracked surface of the alloy, which verifies the good plasticity of the  $Ti_2ZrNbTaMo$  HEA.

Fig. 7 displays the Vickers microhardness of the  $Ti_xZrNbTaMo$  (x=0.5,1,1.5,2) HEAs. With a rise in the Ti content, the hardness values of the Ti-Zr-Nb-Ta-Mo HEAs decrease. It should also be noted that the  $Ti_{0.5}ZrNbTaMo$  alloy has the highest hardness value of about 500 HV. It is reported that the hardness of the biomedical Ti6Al4V alloy is about 320 HV. The results of the hardness testing shows that the Vickers microhardness of the Ti-Zr-Nb-Ta-Mo HEAs is significantly higher than that of the Ti6Al4V alloy, which



 $\textbf{Fig. 6.} \hspace{0.5cm} \textbf{SEM} \hspace{0.5cm} \hspace{0.5cm} \textbf{morphologies} \hspace{0.5cm} \textbf{of} \hspace{0.5cm} \textbf{(a)} - \textbf{(b)} \hspace{0.5cm} \textbf{Ti}_{0.5} \textbf{Z} \textbf{ND} \textbf{TaMo}, \hspace{0.5cm} \textbf{(c)} - \textbf{(d)} \hspace{0.5cm} \textbf{TiZ} \textbf{ND} \textbf{TaMo}, \hspace{0.5cm} \textbf{(e)} - \textbf{(f)} \hspace{0.5cm} \textbf{Ti}_{1.5} \textbf{Z} \textbf{ND} \textbf{TaMo}, \hspace{0.5cm} \textbf{and} \hspace{0.5cm} \textbf{(g)} - \textbf{(h)} \hspace{0.5cm} \textbf{Ti}_{2} \textbf{Z} \textbf{ND} \textbf{TaMo} \hspace{0.5cm} \textbf{HEAs} \hspace{0.5cm} \textbf{after compression deformation.}$ 

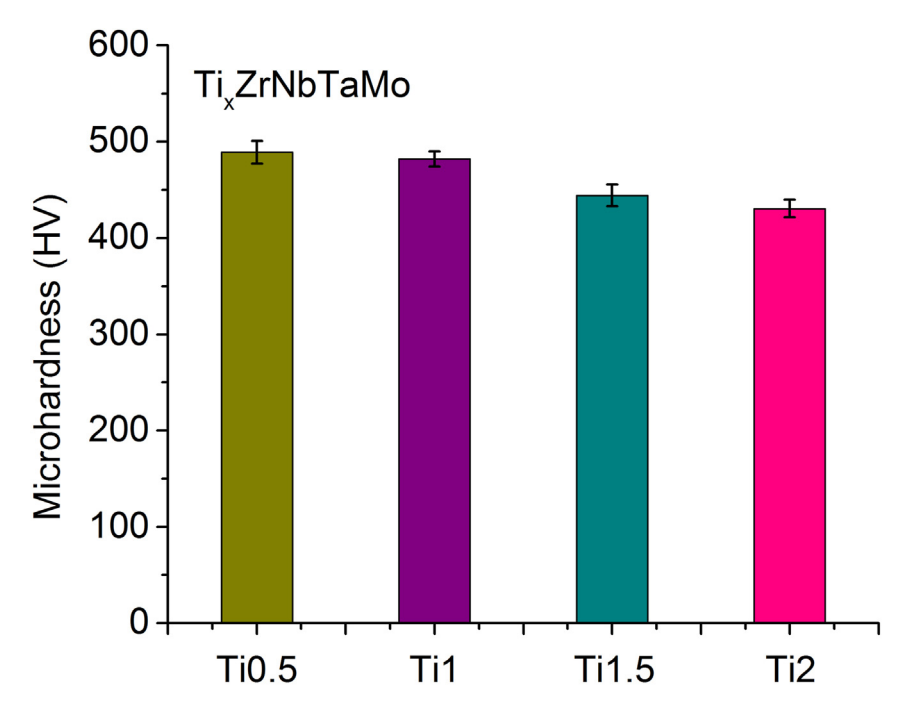
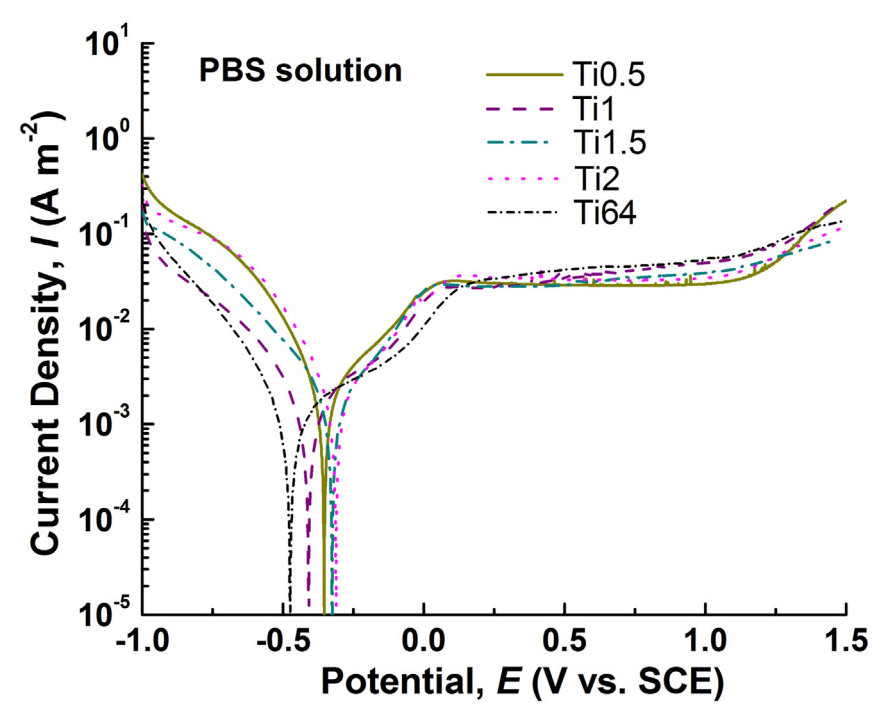


Fig. 7. Vickers microhardness of the  $Ti_xZrNbTaMo~(x=0.5, 1, 1.5, and 2)$  HEAs.

indicates that the HEAs may exhibit superior wear resistance.

Fig. 8 displays the potentiodynamic polarization curves of the  $Ti_xZrNbTaMo$  (x=0.5,1,1.5, and 2) HEAs and Ti6Al4V alloy in the PBS solution. As can be observed, the Ti-Zr-Nb-Ta-Mo HEAs can passivate spontaneously with a low passivation current density on the order of  $10^{-2}$  A m $^{-2}$ . Among those alloys, the  $Ti_{0.5}ZrNbTaMo$  alloy exhibits the lowest passivation current density, which is even lower than that of the Ti6Al4V alloy. Meanwhile, the corrosion potential of all the Ti-Zr-Nb-Ta-Mo HEAs is nobler than that of

the Ti6Al4V alloy, which demonstrates that the passivation film of the HEAs has relatively higher stability. Furthermore, the corrosion current density of the Ti–Zr–Nb–Ta–Mo HEAs is as low as that of the Ti6Al4V alloy, both of which are on the order of  $10^{-3}$  A m<sup>-2</sup>, denoting that the Ti–Zr–Nb–Ta–Mo HEAs show a comparable low corrosion rate to that of the Ti6Al4V alloy. In conclusion, the potentiodynamic polarization curves show that the Ti–Zr–Nb–Ta–Mo HEAs possess the good anti-corrosion property in the PBS solution.



 $\textbf{Fig. 8.} \ \ Potentiodynamic polarization curves of the \ Ti_{x}ZrNbTaMo \ (x=0.5,1,1.5, \ and \ 2) \ \ HEAs \ and \ Ti6Al4V \ alloy in the \ PBS \ solution.$ 

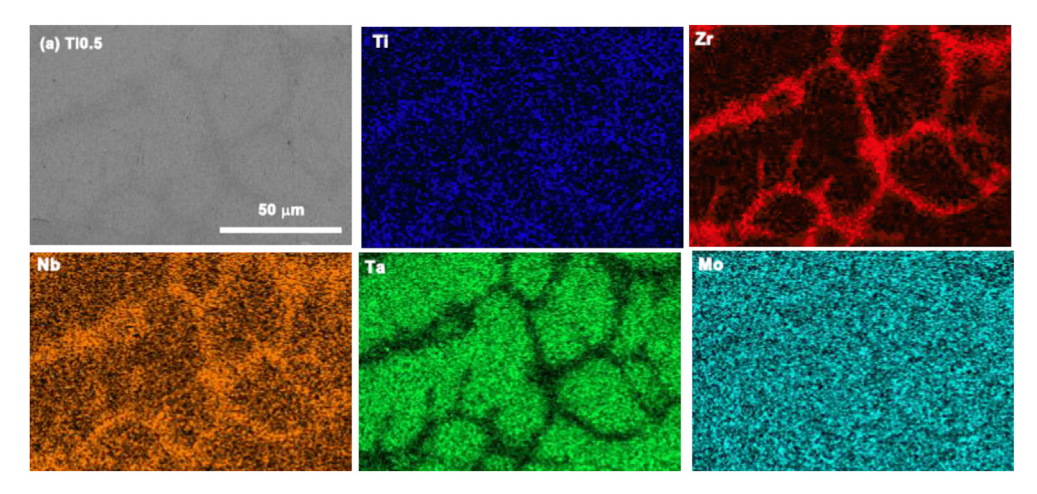


Fig. 9. (a) SEM morphology and EDS compositional distribution mapping of the (b) Ti, (c) Zr, (d) Nb, (e) Ta, and (f) Mo elements on the corroded surface of the Ti<sub>0.5</sub>ZrNbTaMo alloy after potentiodynamic polarization test.

Fig. 9 presents the (a) SEM morphology and EDS compositional distribution mapping of the (b) Ti, (c) Zr, (d) Nb, (e) Ta, and (f) Mo elements on Ti<sub>0.5</sub>ZrNbTaMo HEA surface after the potentiodynamic polarization tests. As can be seen from Fig. 8 (a), no obvious corrosion pits present on the surface of the Ti<sub>0.5</sub>ZrNbTaMo alloy after testing. The surface of the Ti<sub>0.5</sub>ZrNbTaMo alloy clearly exhibits a structure consisting of the coarsened dendrites (light gray contrast) and inter-dendrite matrix (dark gray contrast). Fig. 9(b)—(f) demonstrate that the Ta and Mo elements are enriched in the light gray contrast dendrite region, while the Ti, Zr, and Nb elements are concentrated in the dark gray contrast inter-dendrite matrix region. The compositional distribution of all elements on the surface of the alloy is almost the same as that before the corrosion test. The EDS mapping results for the corroded surface of the other three HEAs exhibit no distinct difference from that of the Ti<sub>0.5</sub>ZrNbTaMo alloy. The above results further confirm that the Ti-Zr-Nb-Ta-Mo HEAs present good anti-corrosion properties in the PBS solution.

To further illustrate the good anti-corrosion property mechanism of the Ti–Zr–Nb–Ta–Mo HEAs, the surface chemistry of the HEAs was examined by XPS. Prior to the XPS tests, the HEA samples were immersed in the PBS solution for 24 h. Fig. 10(a) plots the XPS full spectrum of the surface of the Ti–Zr–Nb–Ta–Mo HEAs, and the narrow scanning spectra of alloy elements Ti, Zr, Nb, Ta, and Mo are shown in Fig. 10(b)–(f). The elemental composition distribution of the alloy surface, as obtained by the XPS analysis, is shown in Fig. 11. As seen in Fig. 10(a), the peaks of the Ti, Zr, Nb, Ta, Mo, C, O, and P elements are present in the full spectrum. The C 1s peak results from the inevitable carbon contamination on the alloy surface.

Fig. 10 displays the narrow scan of the (b) Ti 2p, (c) Zr 3d, (d) Nb 3d, (e) Ta 4f, and (f) Mo 3d of the Ti–Zr–Nb–Ta–Mo HEAs. The Ti 2p peaks of the Ti–Zr–Nb–Ta–Mo HEAs correspond to the Ti<sup>4+</sup> state. As the Ti content increases, the intensity of the Ti 2p peaks enhances significantly. Fig. 10(c) depicts the Zr 3d spectrum, which are ascribed to the Zr<sup>4+</sup> oxidized state. The Nb 3d peaks refer to the states of the Nb<sup>0</sup> and Nb<sup>5+</sup>, as presented in Fig. 10(d). The Ta 4f peaks in Fig. 10(e) correspond to the Ta<sup>0</sup> metallic state and Ta<sup>4+</sup> in the oxidized state. Fig. 10(f) displays the Mo 3d peaks of the metal, Mo<sup>4+</sup>, and Mo<sup>6+</sup> states of the Ti–Zr–Nb–Ta–Mo HEAs. Moreover, the peak intensity of Mo in the metallic state is higher than that of the oxidized state, indicating that the Mo is mainly enriched as the metallic state underneath the passivation film.

Fig. 11 summarizes the XPS results on the surface of the Ti–Zr–Nb–Ta–Mo HEAs. To simplify the comparison of the

elemental concentration on the alloy surface, the data of the C elemental data were removed from the XPS results. It can be found that as the Ti content rises, the fraction of Ti in the surface film of the alloy increases, the fraction of O decreases, and the amount of the Zr, Nb, Ta, and Mo elements do not change significantly. Furthermore, the fraction of O in the Ti<sub>0.5</sub>ZrNbTaMo alloy is the highest among these four HEAs, which indicates more oxide films formed on its surface. Therefore, the passivation film of the Ti<sub>0.5</sub>ZrNbTaMo alloy shows a higher stability, which corresponds to a lower passivation current density.

Fig. 12 shows the (a) wear rates and (b) coefficients of friction for the  $Ti_xZrNbTaMo$  (x = 0.5, 1, 1.5, and 2) HEAs under both dry and wet sliding conditions. As indicated from Fig. 12(a), the dry sliding wear rates of the  $Ti_{0.5}ZrNbTaMo$ , TiZrNbTaMo,  $Ti_{1.5}ZrNbTaMo$ , and Ti<sub>2</sub>ZrNbTaMo HEAs are 2.22  $\times$  10<sup>-7</sup> mm<sup>3</sup> mm<sup>-1</sup> N<sup>-1</sup>, 2.91  $\times$  10<sup>-7</sup> mm<sup>3</sup> mm<sup>-1</sup> N<sup>-1</sup>, and  $2.42 \times 10^{-7} \text{ mm}^3 \text{ mm}^{-1} \text{ N}^{-1}$ , respectively. Importantly, the dry wear rates of the Ti-Zr-Nb-Ta-Mo HEAs are all lower than that of the Ti6Al4V alloy, which is  $3.50 \times 10^{-7} \, \text{mm}^3 \, \text{mm}^{-1} \, \text{N}^{-1}$ . The results show that as the Ti content increases, the wear resistance of the HEAs decreases. Moreover, the Ti<sub>0.5</sub>ZrNbTaMo alloy exhibits the highest wear resistance under dry friction conditions. As for the wet friction conditions, the wear rates of the Ti<sub>0.5</sub>ZrNbTaMo, TiZrNbTaMo, Ti<sub>1.5</sub>ZrNbTaMo, and Ti<sub>2</sub>ZrNbTaMo HEAs under wet friction conditions are  $1.52 \times 10^{-7} \text{ mm}^3 \text{ mm}^{-1} \text{ N}^{-1}$ ,  $1.85 \times 10^{-7} \text{ mm}^3 \text{ mm}^{-1} \text{ N}^{-1}$ ,  $2.27 \times 10^{-7} \text{ mm}^3 \text{ mm}^{-1} \text{ N}^{-1}$ , and  $2.45 \times 10^{-7} \text{ mm}^3 \text{ mm}^{-1} \text{ N}^{-1}$ , respectively. The results indicate, therefore, that the wet wear rates of the Ti-Zr-Nb-Ta-Mo HEAs are all lower than that of the Ti6Al4V alloy, which is  $4.60\times10^{-7}~mm^3~mm^{-1}~N^{-1}.$  It is worth noting that, the wear rates of the Ti-Zr-Nb-Ta-Mo HEAs under wet friction condition is decreased as compared with rates for the dry friction condition. Furthermore, the Ti<sub>0.5</sub>ZrNbTaMo alloy exhibits the largest decrease between the dry and wet wear resistances. This trend proves that the Ti-Zr-Nb-Ta-Mo HEAs show good corrosion resistance under wet friction conditions.

The frictional coefficients for the  $Ti_xZrNbTaMo$  (x=0.5, 1, 1.5, and 2) HEAs that underwent both dry and wet friction conditions are displayed in Fig. 12(b). The results show that the coefficients of friction of the  $Ti_{0.5}ZrNbTaMo$ , TiZrNbTaMo,  $Ti_{1.5}ZrNbTaMo$ , and  $Ti_{2}ZrNbTaMo$  HEAs under the dry wear conditions are 0.75, 0.94, 0.94, and 0.84, respectively. Additionally, the values for the wet friction condition are 0.61, 0.64, 0.71, and 0.71, respectively. In contrast, the frictional coefficients for the Ti6Al4V alloy are 0.61 and

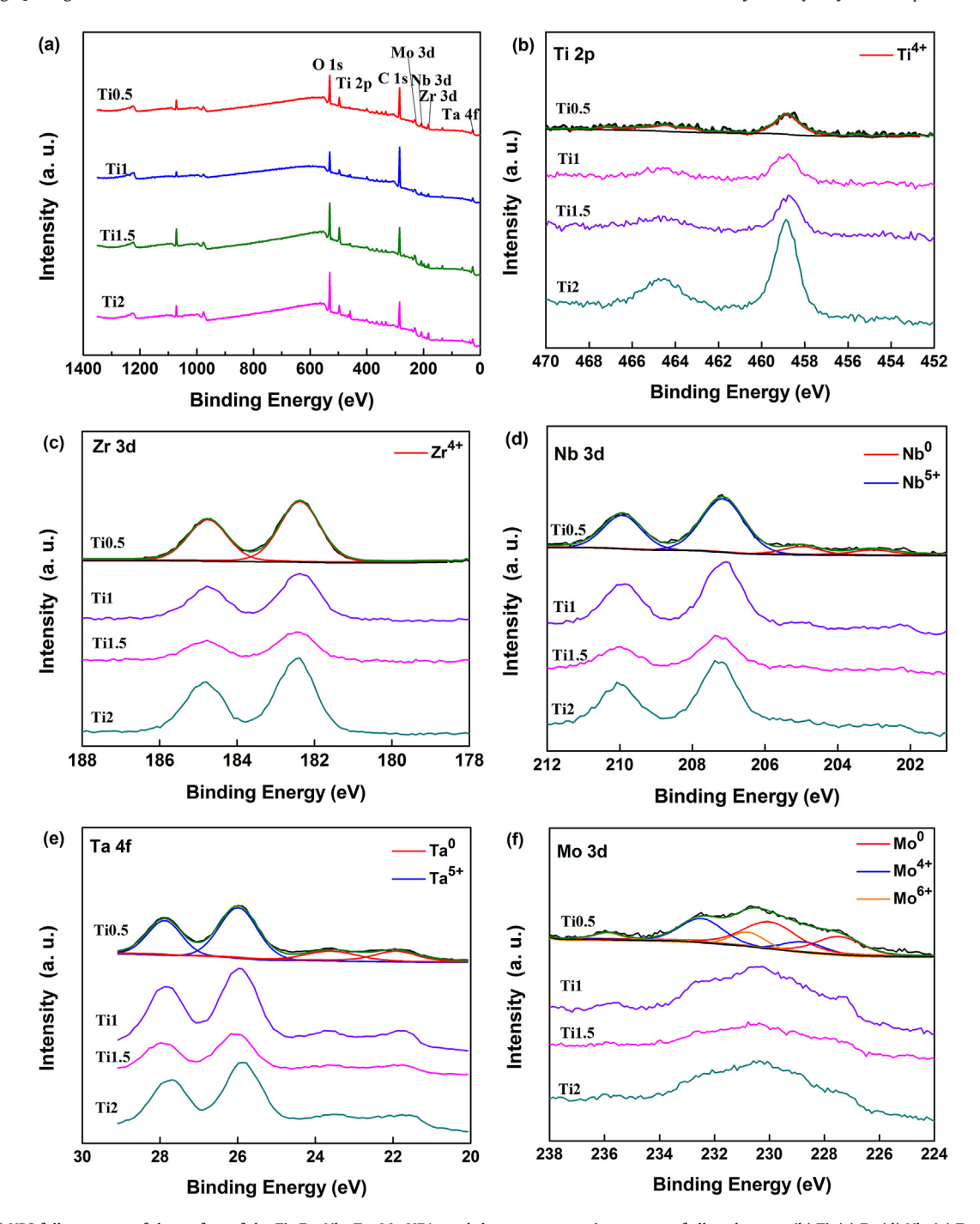


Fig. 10. (a) XPS full spectrum of the surface of the Ti–Zr–Nb–Ta–Mo HEAs and the narrow scanning spectra of alloy elements (b) Ti, (c) Zr, (d) Nb, (e) Ta, and (f) Mo.

0.64, respectively. Obviously, due to the lubrication effect from the aqueous solution, the frictional coefficients of the HEAs decrease when they are under wet sliding conditions. It is of worthy noting that the Ti6Al4V alloy have higher wear rate but lower friction coefficient than the TiZrNbTaMo HEAs. The friction coefficient reflects the lubrication effect of the material. The wear rate corresponds to the material loss. The low friction coefficient of materials do not necessarily mean the low wear rate. This trend is consistence with the previously reported studies [45,47,55].

Fig. 13 exhibits the SEM surface morphologies of the wear scars for the (a) - (c)  $Ti_{0.5}ZrNbTaMo$ , (d) - (f) TiZrNbTaMo, (g) - (i)  $Ti_{1.5}ZrNbTaMo$ , and (j) - (l)  $Ti_2ZrNbTaMo$  HEAs under the dry wear

condition. The wear surfaces of the HEA specimens are composed of two areas with different contrasts. The discontinuous irregular island shape region shows a black contrast, while the other area of the wear scar surface between the island-like convexity exhibits a white contrast. It can be seen that there are grooves parallel to the friction direction, which is a typical feature of the abrasive wear [28–32].

The results of the EDS analysis of the black and white contrast regions are shown in Fig. 13(m). The findings indicate that the elemental composition of the wear scar surface of the HEAs is consists of the Ti, Zr, Nb, Ta, Mo, and O. Here, the black-island-shaped region displays a high content of O, while the gray white

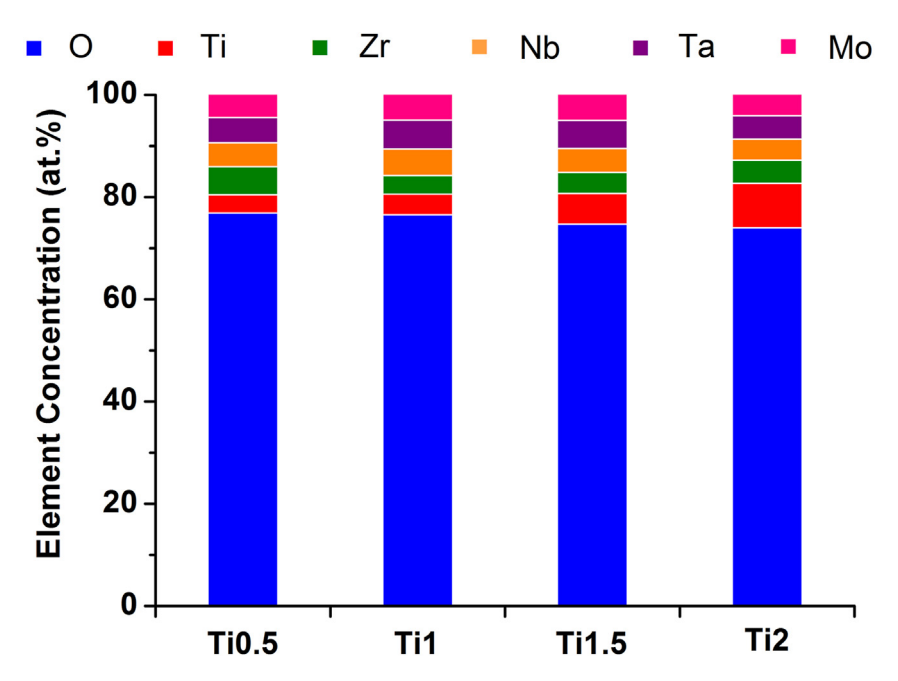


Fig. 11. XPS results of on the surface of the Ti-Zr-Nb-Ta-Mo HEAs.

surface region presents a low content of O. The results, as seen in Fig. 13(m), suggest that the black-island-shaped region (which contains obvious cracks on its surface, for example in Fig. 13(c)) consists of various oxides, such as TiO2, ZrO2, and Nb2O5. The surface oxidation that occurs in the Ti-Zr-Nb-Ta-Mo HEAs during the dry friction and wear process is mainly due to the oxygen affinity elements (such as Ti and Zr) that easily react with O in the air. From the viewpoint of friction, the high hardness of the oxides decreases the frictional coefficient and thus enhances the wear resistance of the HEAs. However, the oxides are brittle. For instance, the TiO<sub>2</sub> is highly susceptible to cracking under an applied stress due to its low fracture toughness. Under the reciprocating sliding friction, the surfaces of the Ti-Zr-Nb-Ta-Mo HEAs may form complex oxides which are easy to crack and peel off. The flake-like wear debris is crushed repeatedly and refined into many oxide particles. These high hardness particles will scrape the fresh metal surface, causing three-body wear that may accelerate the material degradation of the alloys [45,46]. In conclusion, the results indicate that the wear mechanism of the Ti-Zr-Nb-Ta-Mo HEAs under the dry friction condition is the abrasive wear and oxidation wear. With the rise in the Ti content for the HEAs, more TiO<sub>2</sub> oxides will form during the sliding process, resulting in both the serious oxidation wear and lower wear resistance.

Fig. 14 exhibits the SEM images of the surface wear scars for the (a) - (c)  $Ti_{0.5}ZrNbTaMo$ , (d) - (f) TiZrNbTaMo, (g) - (i)  $Ti_{1.5}ZrNbTaMo$ , and (j) - (l) Ti<sub>2</sub>ZrNbTaMo HEAs under the wet friction condition. The compositional analysis results for the different regions of the wear scar surfaces are listed in Fig. 14(m). It was found that the wear scar morphologies under the dry friction condition were similar to those for the wet friction condition in the PBS solution, such as the presence of two distinct areas in the wear scars of the HEAs with different surface contrasts. The EDS analysis results show that the black contrast area contains a high oxygen content, which results from the corrosion reaction during the process of wet friction. Parallel grooves on the surface of the gray white contrast area were also observed, which is due to the abrasive wear caused by the high hardness oxide particles that peeled off from the corrosion product layer. In conclusion, the wear mechanism of the Ti-Zr-Nb-Ta-Mo HEAs under the wet friction condition consists of both abrasive

wear and corrosion wear.

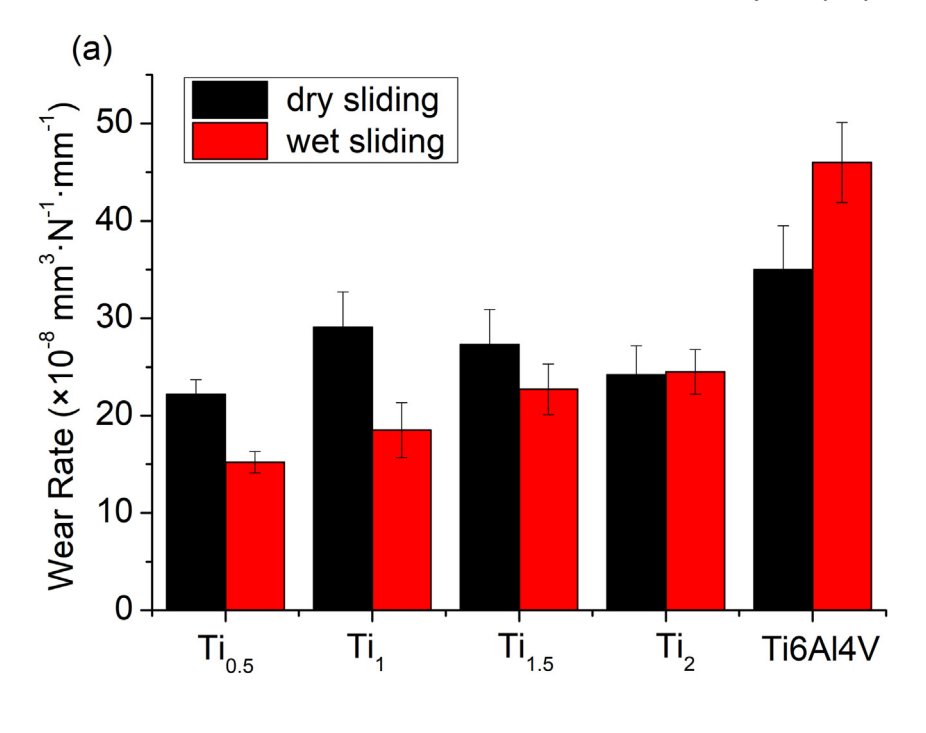
#### 4. Discussion

Metallic materials have been widely employed in the field of orthopedic implant materials owing to their excellent mechanical properties, for instance, the good strength, plasticity, fatigue strength, and fracture toughness. The ideal materials for

Orthopedic implants, such as those used for articular support surface applications, should have several characteristics. For instance, low chemical toxicity and excellent corrosion resistance in physiological environments as to avoid adverse reactions in recipient tissues [1–3,24,25]. Moreover, good wear resistance arising from a small friction coefficient and good lubrication of the synovium prevents the protein degeneration of the synovium [4,5]. Furthermore, high hardness and strength can avoid the deformation of joint surfaces under high loads [47,48].

Very recently, a number of TiZr-based refractory HEAs, including the Ti-Zr-Hf-Nb [20,21], Ti-Zr-Nb-Ta [22], Ti-Zr-Hf-Nb-Mo [23], Ti-Zr-Nb-Ta-Mo [24,25], Ti-Zr-Hf-Nb-Ta [26,27] and Hf-Mo-Nb-Ta-Ti-Zr [28] HEA systems, have been studied to assess their suitability for orthopedic implants, and quite encouraging results were obtained. Generally, these TiZr-based refractory HEAs have BCC solid solution phase structure. For instance, the Ti-Zr-Hf-Nb, Ti-Zr-Nb-Ta, and Ti-Zr-Hf-Nb-Ta had a single BCC solid solution structure with no formation of any second phase [20-22,26,27]. Typical dendritic morphology was observed in the alloys enriched in Nb and Ta, while the inter-dendrite contains a high concentration of Ti and Zr, manifesting occurrence of elemental segregation during solidification [20–22,26,27]. In the present study, the Ti-Zr-Nb-Ta-Mo HEAs have a dendrite structure that is composed of two BCC solid solution phases, which is consistent with the structure results of previously reported studies [24,25]. The TiZrNbTaMo HEA exhibits a fine dendrite structure. With decreasing Ti content, the Ti<sub>0.5</sub>ZrNbTaMo HEA shows an obviously coarsened dendrite arm structure. The increase in the Ti content results in the formation of short and spherical dendrite arms for the Ti<sub>2</sub>ZrNbTaMo HEA.

Owing to the BCC dendrite structure, TiZr-based refractory HEAs



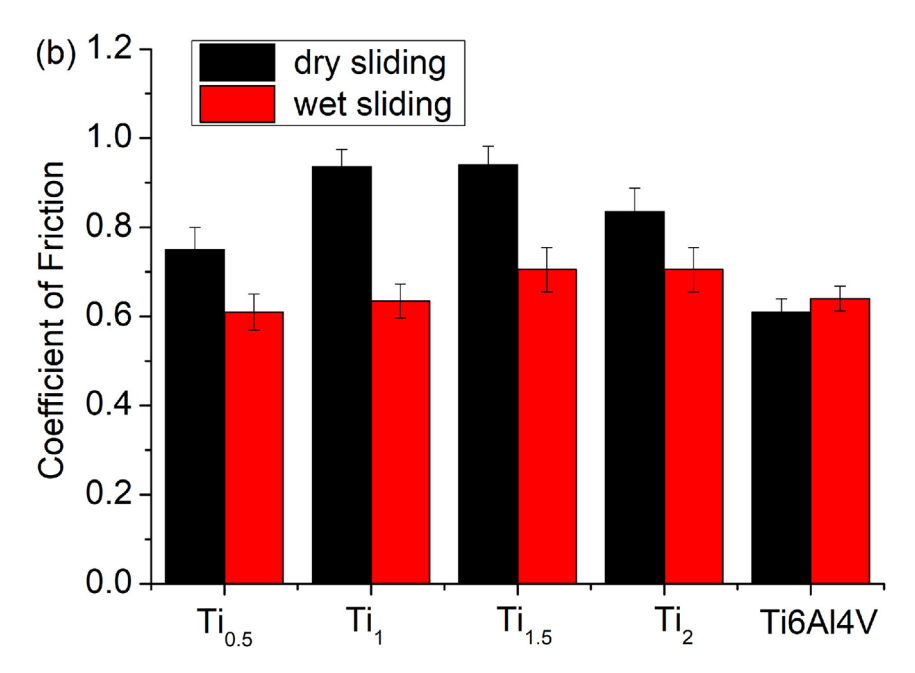
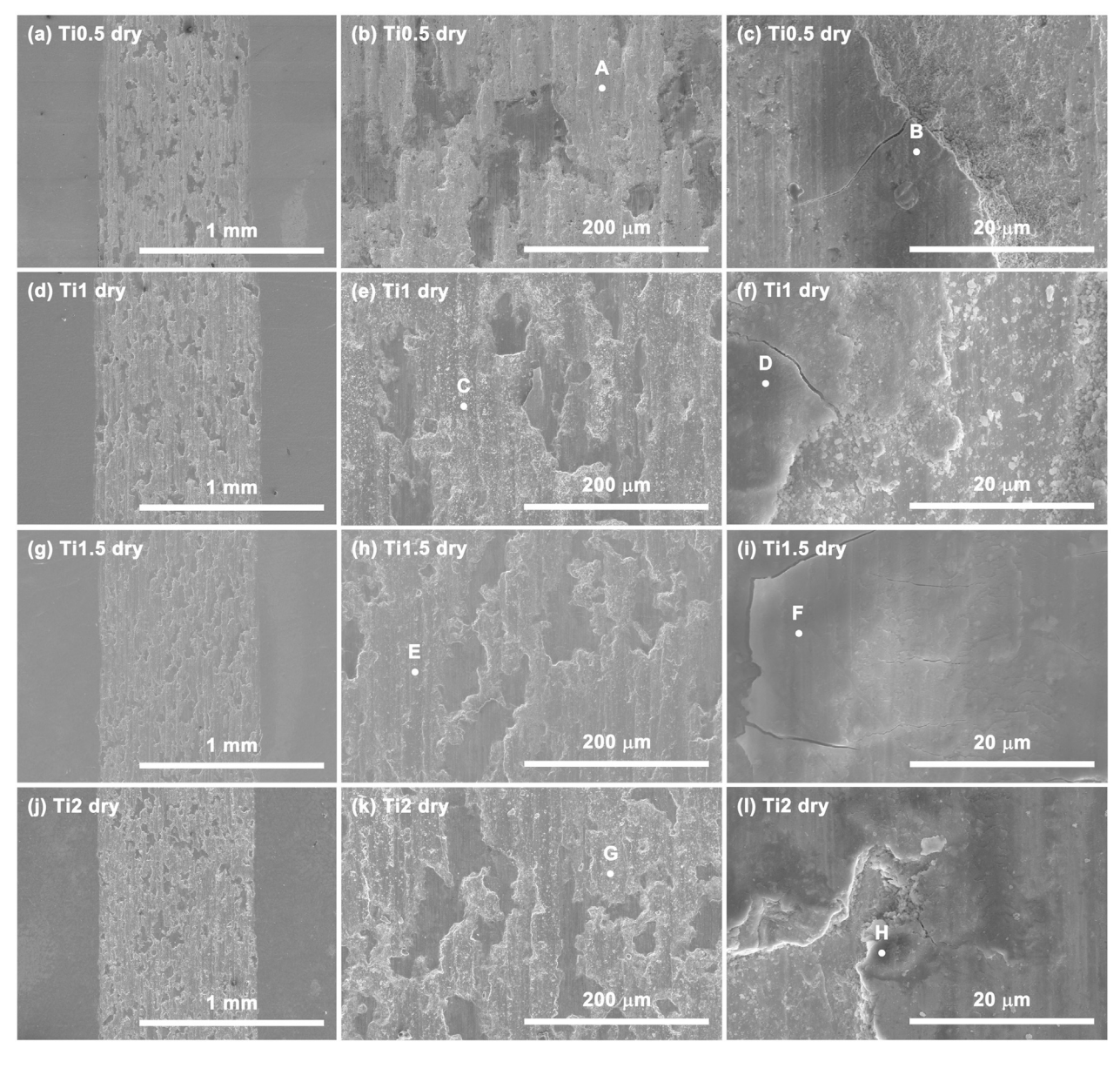


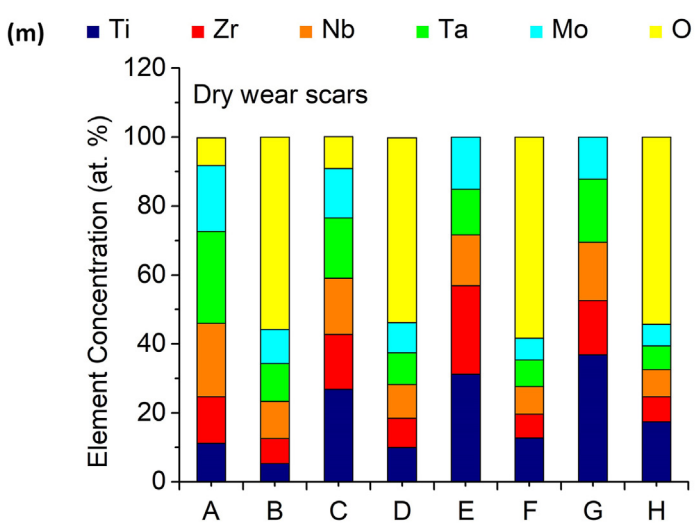
Fig. 12. (a) Wear rates and (b) coefficients of friction of the Ti<sub>x</sub>ZrNbTaMo (x = 0.5, 1, 1.5, and 2) HEAs under dry and wet sliding in the PBS solution, respectively.

display high yield strength ( $\sigma_y = 900-1600$  MPa) at ambient temperature, among which someone manifests sizable compressive plasticity. It has been reported that the equimolar TiZrHfNbTa HEA exhibited high yield strength (800-985 MPa) and low elastic modulus ( $\sim$ 80 GPa). Furthermore, the TiZrHfNbTa HEA possessed a low passive current density of about  $10^{-2}$  A/m², a low corrosion rate in the order of  $10^{-4}$  mm/year in the Hank's solution at 310 K, and displayed as good bio-corrosion resistance as that of the Ti6Al4V alloy [49]. Besides, the good adhesion, viability and proliferation behaviors of MC3T3-E1 pre-osteoblasts on the TiZrHfNbTa HEA indicated its good *in vitro* biocompatibility [49]. Recent studies have

reported the equiatomic Ti—Nb—Zr—Ta—Mo HEA for biomedical applications [24,25]. This HEA showed high compressive yield strengths up to 1400 MPa and high microhardness of 4.9 GPa [24,25]. However, the wear and corrosive wear properties of the TiZrNbTaMo HEA is still unknown. Thus, in the present study, we investigate the wear and corrosive wear behaviors of the equiatomic and nonequiatomic Ti—Zr—Nb—Ta—Mo HEAs and found that they possess better corrosive wear resistance than that of the conventional biomedical Ti—6Al—4V alloy, which may reduce the risk of the "particle disease".

The findings of this study indicate that as compared to the





traditional biomedical implant material Ti6Al4V alloy, the Ti–Zr–Nb–Ta–Mo system HEAs would perform better in biological environments. This relatively better performance is attributed to the high strength, high hardness, exceptional biocompatibility, good anti-corrosion and -wear properties. Therefore, the Ti–Zr–Nb–Ta–Mo system HEAs is a promising candidate material for application in the field of orthopedic implant materials.

#### 4.1. Wear resistance of the Ti-Zr-Nb-Ta-Mo HEAs

Traditional Ti-based alloys usually show poor wear resistance, which may induce the "particle disease" caused by the abrasive particles. Moreover, the precipitation of biologically toxic Al and V ions that results from the effects of corrosion and wear can affect their biosafety and service life [4,5]. Because of their unique glassy structures, the strength and hardness of the Ti-based metallic glasses are 2-3 times those of crystalline titanium alloys. Therefore, the Ti-based metallic glasses often show the high wear resistance under dry friction. However, because most of the Tibased metallic glasses contain a high amount of Cu element, pitting corrosion will most likely occur in the physiological solution. The pitting corrosion usually results in the corrosive wear, which leads to the low wear resistance under wet friction conditions. Furthermore, the limited dimensions of metallic glasses and the poor tensile plasticity restrict their application as biomedical implant materials [6-10].

Due to their multi-principal component characteristics, HEAs exhibit good properties such as high strength and hardness, as well as good anti-wear capacity; and have attracted the extensive attention of researchers. As potential engineering materials, HEAs possess excellent friction and wear behaviors that are needed for long-term service reliability [11-14]. For orthopedic implant materials, high wear resistance can reduce the risk of "particle disease" that is caused by friction and wear. Fig. 15 summarizes the relationship between the wear coefficient,  $R_{w}$ , and the hardness,  $H_{v}$ , for various HEAs. Furthermore, the data of the Ti6Al4V alloy is also plotted for comparison. It can be seen from Fig. 15 that the wear resistance coefficient of the various HEAs covers a range spanning more than three orders of magnitude [32,50-52]. For example, the hardness value of the Mo-Ta-W-Nb-V HEA is as high as 700 HV, and the wear resistance coefficient reaches to 10<sup>13</sup> Pa. In contrast, the hardness value of the Co-Cr-Fe-Mn-Ni HEA is as low as ~200 HV, and the wear resistance coefficient is only 10<sup>11</sup> Pa [31,52].

According to the Achard's wear law [53], the wear resistance of the material is directly proportional to its hardness. Thus, increasing the hardness of the material can improve its ability to resist the compression deformation, thereby enhancing improve its wear resistance. Moreover, investigations have found that the fracture toughness of the material also has a remarkable influence on the wear behavior. For instance, enhancing the fracture toughness of a material can increase the ability to resist crack nucleation and propagation, resulting in an improved wear resistance of the material [53-55]. For the crystalline metallic materials, which usually show signs of excellent toughness, their wear resistance is often controlled by the hardness. For the brittle ceramic or glass materials, the fracture toughness often plays a dominant role in controlling the wear resistance. It can be seen from Fig. 15 that the displayed trends in the wear resistance for the HEAs generally agrees with the Archard's wear law, that is, the wear resistance of the material enhances as the hardness increases. In this study, the hardness of the Ti-Zr-Nb-Ta-Mo HEA is 500 HV while wear

resistance coefficient is  $4.5 \times 10^{12}$  Pa, indicating that its wear resistance is higher than that of the Ti6Al4V alloy and the most of the other HEAs featured in Fig. 15.

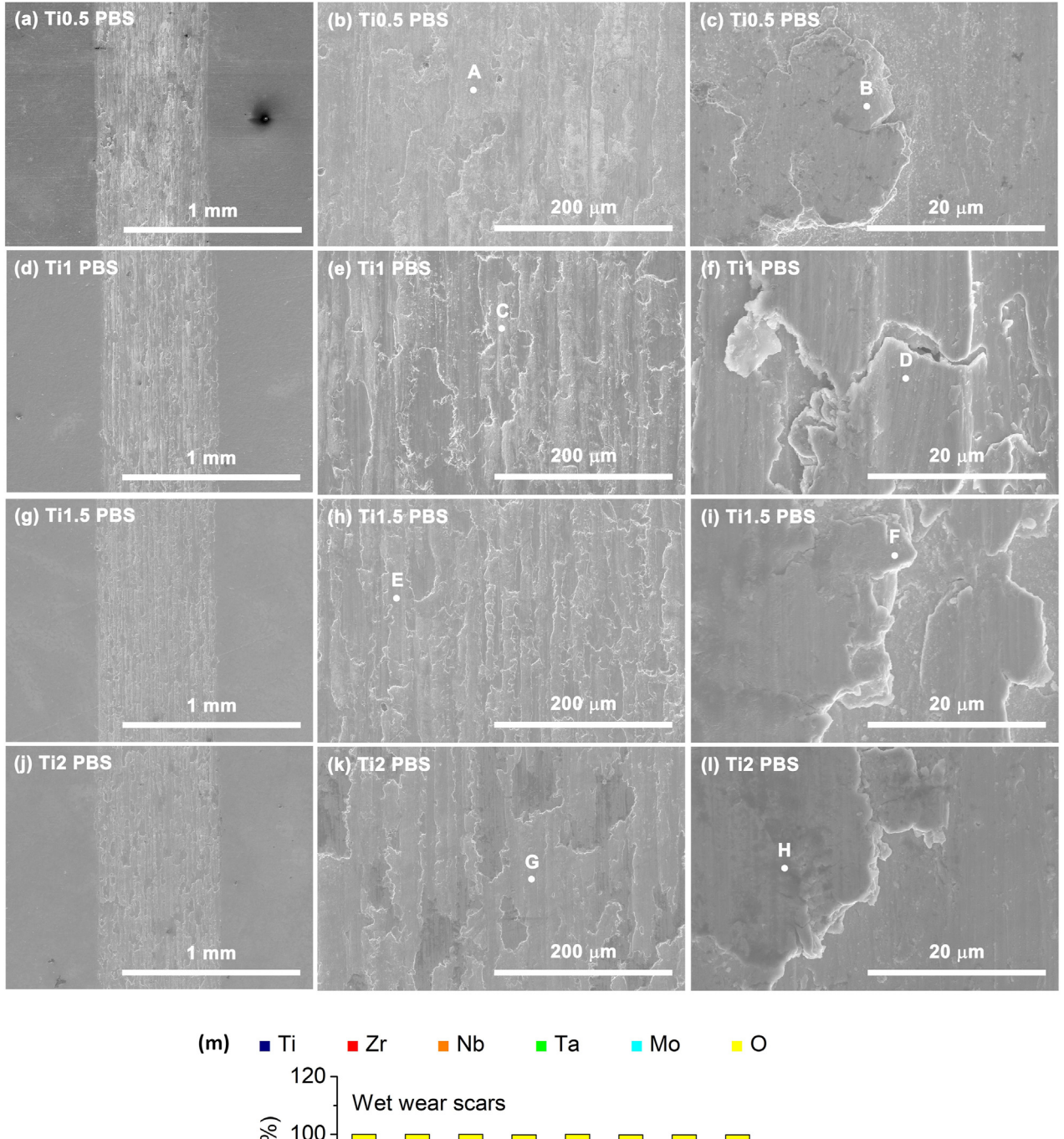
The mechanical properties of the HEAs are affected by their structures. Owing to factors, such as the high-configurationalentropy-, lattice-distortion-, and sluggish-diffusion-effects, that result from the multi-principal component characteristics, the HEAs usually exhibit a simple FCC, BCC, or HCP solid solution structure [11–14]. Furthermore, the HEAs with the BCC structure usually have high hardness but low plastic deformation ability. Meanwhile, the FCC HEAs tend to display good plastic deformation behavior but low hardness. The HEAs with the mixture of BCC and FCC structures, on the other hand, may have a balanced combination of strength and fracture toughness that results in good comprehensive mechanical properties [11–14]. Unfortunately, the reported data regarding the friction and wear behavior of the HEAs is insufficient since different test conditions were used by the various institutions when investigating these phenomena. Thus, the friction and wear behaviors, as well as the wear mechanisms of the HEAs, requires further investigation.

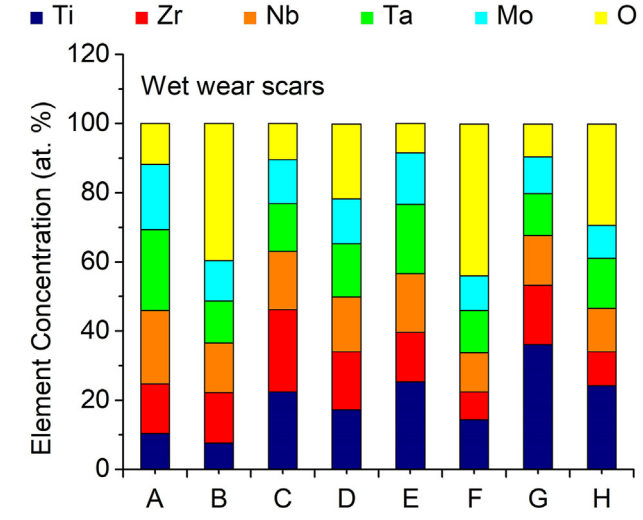
It is known that with a rise in the Ti content, the hardness values of the Ti–Zr–Nb–Ta–Mo HEAs decrease. According to the classical wear theory, high hardness a material may reduce the plastic deformation on the material surface, and thus prevent the formation of microcracks [53,54]. Generally, the decrease in the hardness will reduce the wear resistance. Moreover, according to the XPS analysis of this study, with increasing Ti, more TiO<sub>2</sub> formed on the surface. However, TiO<sub>2</sub> is known to be easily peeled-off from the surface layer, which is detrimental to the wear resistance. In the present study, it is suggested that both factors take effects on the decrease in the wear resistance of the Ti–Zr–Nb–Ta–Mo HEAs.

# 4.2. Corrosive wear behaviors of the Ti-Zr-Nb-Ta-Mo HEAs

It is indicated from Fig. 12(a) and (b) that the wear rates of the Ti-Zr-Nb-Ta-Mo HEAs under the wet wear are lower than that of the dry wear condition. This result indicates that the corrosion in the PBS solution has no significant accelerating influence on wear. The wear rate of the Ti6Al4V alloy, while undergoing sliding in the PBS solution, is slightly higher than that of the dry wear, suggesting that there is a certain degree of the corrosion wear interaction that occurs during the process of wet friction. When metallic implant materials are present in the human body, they are commonly exposed to both the wear and corrosion effects [56,57]. The combined effects of the wear and corrosion usually significantly accelerates the wear loss of materials. There are several investigations which report the corrosion and wear behavior of crystalline metallic materials, where the interaction mechanism of the corrosion and wear was summarized. The findings of these studies indicate that the mechanisms of the wear-accelerated corrosion are: the damage of passivation films; plastic deformation results in the multiplication of dislocations and vacancies; the surface roughening of the material [58,59]. Additionally, the mechanisms of corrosion-accelerated wear mainly include: the multiplication of porosity and corrosion products; the deterioration in the bonding strength due to the grain-boundary-corrosion; the environmentinduced-brittleness [60,61].

As observed from Fig. 8, the Ti–Zr–Nb–Ta–Mo HEAs show similarly low corrosion current density values in the PBS solution as the Ti6Al4V alloy, indicates that the HEAs has a low corrosion rate. Furthermore, the Ti–Zr–Nb–Ta–Mo HEAs exhibit higher corrosion





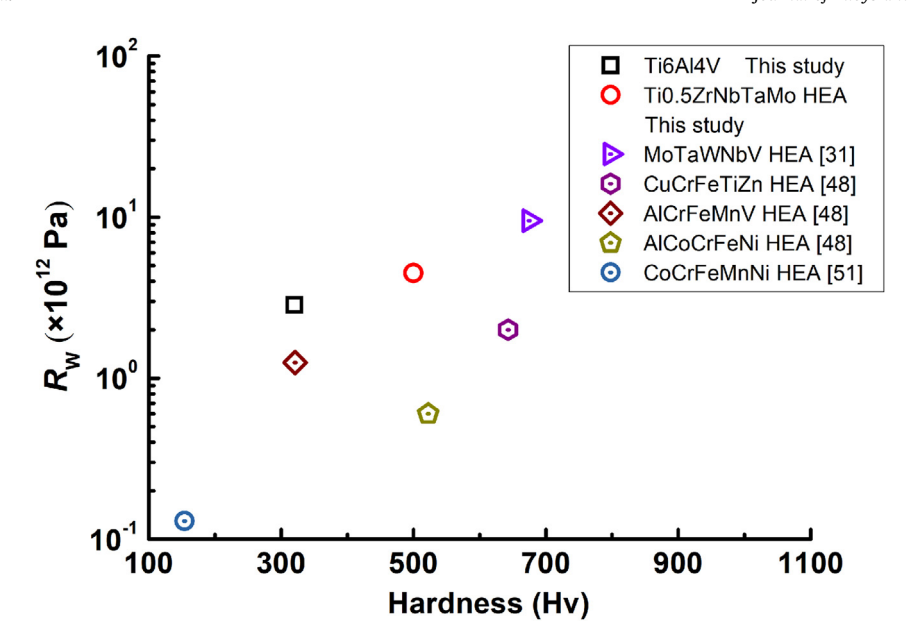


Fig. 15. The relationship between the wear coefficient,  $R_{wv}$  and the hardness,  $H_{vv}$  of various HEAs and the Ti6Al4V alloy.

potentials than that of the Ti6Al4V alloy, which demonstrates the higher passivation film stability of the HEAs. The Ti–Zr–Nb–Ta–Mo HEAs also display good corrosion resistance, which is related to the chemical composition and microstructure of the surface. According to the analytical results from the XPS experiment, as displayed in Fig. 10, the metallic elements, such as the Ti, Zr, Nb, Ta, and Mo, are present in the surface structure of the HEAs in two states. One is the oxidation state in the surface film and the other is the metal state below the surface film. Furthermore, the surface film of the alloy is mainly composed of the Ti<sup>4+</sup>, Zr<sup>4+</sup>, Nb<sup>5+</sup>, Ta<sup>5+</sup>, Mo<sup>4+</sup>, and Mo<sup>6+</sup> oxides. It can be seen from Fig. 11 that with the decrease in the Ti content of the HEAs, the oxygen content in the surface film increases, the fraction of Ti<sup>4+</sup> decreases, and the fraction of Nb<sup>5+</sup>, Ta<sup>5+</sup>, Mo<sup>4+</sup>, and Mo<sup>6+</sup> increases gradually.

Previous studies have shown that the  $TiO_2$ ,  $ZrO_2$ ,  $Nb_2O_5$ ,  $Ta_2O_5$ , and  $MoO_3$  oxides with a stable chemical state are all conducive to the formation of continuous, stable, and protective passive films [62-64]. It was also reported that the presence of  $Nb^{5+}$  ions increased the amount of oxygen ions, which may eliminate the anion vacancy and reduce the defects in the passive films. Importantly, the disappearance of anion vacancies reduced the diffusion rate of the passivation layer, resulting in an improvement of the corrosion resistance. Moreover, the existence of the metal state, Ta, was also observed on the surface of the alloy. The presence of the metallic Ta is a unique feature of the protective passivation surface film formed on the Ta-based alloys.

The findings of the present investigation also suggest that the surface chemical structure of the Ti–Zr–Nb–Ta–Mo HEAs contributes to their good corrosion behavior in the PBS solution. The resistance to corrosion in the PBS solution is attributed to the absence of any corrosion-accelerate-wear effect in the allotted time range for the wear tests in this study. Furthermore, the PBS solution plays a lubricating role that leads to a reduction in the friction coefficient as well as a decrease of wear loss. Consequently, the Ti–Zr–Nb–Ta–Mo HEAs exhibit good anti-corrosive-wear property in the PBS solution.

# 4.3. Biocompatibility of the Ti-Zr-Nb-Ta-Mo HEAs

In the past decade, owing to their good mechanical properties and high corrosion resistance, HEAs with multi-principal components have attracted wide attentions in the field of biomedical implant materials [9–14]. Among them, the Ti-Zr-Hf-Nb [20,21], Ti-Zr-Nb-Ta [22], Ti-Zr-Hf-Nb-Mo [23], Ti-Zr-Nb-Ta-Mo [24,25], Ti-Zr-Hf-Nb-Ta [26,27] and Hf-Mo-Nb-Ta-Ti-Zr [28] HEA systems have a BCC solid solution structure and exhibit high yield strengths (900-1,600 MPa), which are helpful in reducing both the sizes of implant materials as well as the biological tissue damage during operation [47]. Meanwhile, some HEAs show good plasticity under compression [20-28]. The studies on the biological corrosion behavior and biocompatibility of the BCC-structured HEAs show that most of these alloys show as high of a corrosion resistance as the pure titanium or Ti6Al4V alloy in physiological environments. To some extent, the biocompatibility of biomedical metallic materials is determined by their corrosion resistance. Due to the longterm operation of implant alloys in the corrosive human body fluids, high corrosion resistance plays an important role in preventing the release of toxic metal ions, and also ensures the good mechanical properties of implant materials in corrosive human body [33–35].

From the perspective of biocompatibility, most of the components of these HEAs have high biosafety [24–26]. Metallic implant materials will release metal ions, such as the zirconium, niobium, and tantalum ions, in the corrosive body fluids. Since the active ions immediately combine with water molecules or anions, there is less toxicity due to the combination with biomolecules, thus showing high biocompatibility. Yang et al. [49] studied the cell adhesion and proliferation behaviors of the MC3T3-E1 osteoblasts on the surface of the Ti–Zr–Nb–Ta-Hf HEA with equal atomic ratio. The results showed that the cell adhesion and proliferation behaviors on the surface of the Ti–Zr–Nb–Ta-Hf HEA were not significantly different from that of the Ti6Al4V alloy, indicating that it has good biocompatibility. Due to the higher corrosion resistance of Mo than

that of Hf in the corrosive body fluids, Todai et al. [24] studied the adsorption and proliferation behaviors of mouse osteoblasts on the surface of the equal-atomic-ratio Ti–Zr–Nb–Ta-Hf HEA, and found that the HEA has better cell compatibility than that of pure Ti and 316L stainless steel. In this study, the non-equimolar Ti<sub>0.5</sub>ZrNbTaHf HEA has higher corrosion resistance and better biocompatibility, which lays a foundation for future applications as biomedical implant materials.

#### 5. Conclusion

The mechanical, corrosion, and wear behaviors of a series of biomedical Ti–Zr–Nb–Ta–Mo HEAs were investigated in this study. The main conclusions are as follows:

- 1. The Ti–Zr–Nb–Ta–Mo HEAs have a dendrite structure that is composed of two BCC solid solution phases. In addition, the TiZrNbTaMo HEA exhibits a fine dendrite structure. In contrast, the Ti<sub>0.5</sub>ZrNbTaMo HEA shows an obviously coarsened dendrite structure. The increase in the Ti content results in the formation of short and round dendrite arms for the Ti<sub>2</sub>ZrNbTaMo HEA.
- 2. With the decrease in the Ti content of the Ti–Zr–Nb–Ta–Mo HEAs, the Vicker's microhardness of the alloys increases from 450 HV to 500 HV, and yield strength increases from 1,440 MPa to 1,580 MPa. Moreover, the Ti<sub>0.5</sub>ZrNbTaMo alloy that exhibits a coarsened dendrite structure shows a high compressive strength of 2,600 MPa together with a good plastic deformation strain approaching 30%.
- 3. The Ti–Zr–Nb–Ta–Mo HEAs display as low of a corrosion current density in the PBS solution as that of the Ti6Al4V, indicating a low corrosion rate for the HEAs. Moreover, the Ti–Zr–Nb–Ta–Mo HEAs have better corrosion potentials than that of the Ti6Al4V alloy, which demonstrates that the HEAs have a relatively higher passivation film stability. The XPS results reveal that the surface film of the HEAs is mainly composed of the Ti<sup>4+</sup>, Zr<sup>4+</sup>, Nb<sup>5+</sup>, Ta<sup>5+</sup>, Mo<sup>4+</sup>, and Mo<sup>6+</sup> oxides, which contribute to the good corrosion resistance of the HEAs in the PBS solution
- 4. The Ti–Zr–Nb–Ta–Mo HEAs exhibit superior dry- and wetwear resistance to that of the Ti6Al4V alloy. With the decrease in the Ti content, the wear resistance of the HEAs enhances. The wear rates of the Ti–Zr–Nb–Ta–Mo HEAs under the wet friction condition are decreased compared with those of the dry friction condition. Finally, the Ti<sub>0.5</sub>ZrNbTaMo alloy exhibits the best corrosive wear resistance among the four HEAs.

# Data availability

The raw/processed data required to reproduce these findings cannot be shared at this time as the data also forms part of an ongoing study.

#### **CRediT authorship contribution statement**

Nengbin Hua: Conceptualization, Methodology, Writing - review & editing, Writing- Reviewing and Editing. Wenjie Wang: Investigation, Data curation, Writing - original draft, preparation. Qianting Wang: Writing - review & editing, Writing- Reviewing and Editing, Youxiong Ye: Formal analysis, Structural analysis. Sihan Lin: Formal analysis, XPS data analysis. Lei Zhang: Investigation, Data curation. Qiaohang Guo: Investigation, Resources.

**Jamieson Brechtl:** Writing - review & editing, Writing- Reviewing and Editing. **Peter K. Liaw:** Writing- Reviewing and Editing, Writing - review & editing.

### **Declaration of competing interest**

The authors declare that they have no known competing financial interests or personal relationships that could have appeared to influence the work reported in this paper.

#### Acknowledgement

The present work was supported by the National Natural Science Foundation of China (21701024), the Natural Science Foundation of Fujian Province (2018J01629), the New Century Excellent Talents in University of Fujian Province (GY-Z17066), and the Scientific Research Project of Fujian University of Technology (GY-Z17152). P.K.L. very much appreciates the supports from (1) the National Science Foundation DMR-1611180 and 1809640 with program directors, Drs. J. Yang, G. Shiflet, and D. Farkas and (2) the US Army Research Office Project nos. W911NF-13–1-0438 and W911NF-19–2-0049 with program managers, Drs. M.P. Bakas, S.N. Mathaudhu, and D.M. Stepp.

#### References

- M.J. Yaszemsk, D.J. Trantolo, K.U. Lewandrowski, V. Hasirci, D.E. Altobelli, D.L. Wise, Biomaterials in Orthopedics, Marcel Dekker Inc., NY, 2004.
- [2] Q.Z. Chen, G.A. Thouas, Metallic implant biomaterials, Mater. Sci. Eng. R 87 (2015) 1–57, https://doi.org/10.1016/j.mser.2014.10.001.
- [3] M. Geetha, A.K. Singh, R. Asokamani, A.K. Gogia, Ti based biomaterials, the ultimate choice for orthopaedic implants - a review, Prog. Mater. Sci. 54 (2009) 397–425, https://doi.org/10.1016/j.pmatsci.2008.06.004.
- [4] M.A. Hussein, A.S. Mohammed, N. Al-Aqeeli, Wear characteristics of metallic biomaterials: a review, Materials 8 (2015) 2749–2768, https://doi.org/ 10.3390/ma8052749
- [5] M.Z. Ibrahim, A.A.D. Sarhan, F. Yusuf, M. Hamdi, Biomedical materials and techniques to improve the tribological, mechanical and biomedical properties of orthopedic implants –A review article, J. Alloys Compd. 714 (2017) 636–667, https://doi.org/10.1016/j.jallcom.2017.04.231.
- [6] W.H. Wang, C. Dong, C.H. Shek, Bulk metallic glasses, Mater. Sci. Eng. R 321 (2008) 502–503, https://doi.org/10.1016/j.mser.2004.03.001.
- [7] G. Pan, D. Lei, J. Jin, X. Wang, S. Wang, Review on the research and development of Ti-based bulk metallic glasses, Metals 6 (2016) 264–301, https://doi.org/10.3390/met6110264.
- [8] S. Pang, Y. Liu, H. Li, L. Sun, Y. Li, T. Zhang, New Ti-based Ti-Cu-Zr-Fe-Sn-Si-Ag bulk metallic glass for biomedical applications, J. Alloy, Compd 625 (2015) 323–327, https://doi.org/10.1016/j.jallcom.2016.03.224.
- [9] H.T. Duan, J.S. Tu, S.M. Du, H.C. Kou, Y. Li, J.P. Wang, Z.W. Chen, J. Li, Tribological properties of Ti<sub>40</sub>Zr<sub>25</sub>Ni<sub>8</sub>Cu<sub>9</sub>Be<sub>18</sub> bulk metallic glasses under different conditions, Mater. Des. 32 (2011) 4573–4579, https://doi.org/10.1016/i.matdes.2011.04.018.
- [10] M.L. Rahaman, L.C. Zhang, H.H. Ruan, Effects of environmental temperature and sliding speed on the tribological behaviour of a Ti-based metallic glass, Intermetallics 52 (2014) 36–48, https://doi.org/10.1016/j.intermet. 2014.03.011.
- [11] J.W. Yeh, S.K. Chen, S.J. Lin, J.Y. Gan, T.S. Chin, T.T. Shun, C.H. Tsau, S.Y. Chang, Nanostructured high-entropy alloys with multiple principal elements: novel alloy design concepts and outcomes, Adv. Eng. Mater. 6 (2004) 299–303, https://doi.org/10.1002/adem.200300567.
- [12] Z.P. Lu, H. Wang, M.W. Chen, I. Baker, J.W. Yeh, C.T. Liu, T.G. Nieh, An assessment on the future development of high-entropy alloys: summary from a recent workshop, Intermetallics 66 (2015) 67–76, https://doi.org/10.1016/j.intermet.2015.06.021.
- [13] D.B. Miracle, O.N. Senkov, A critical review of high entropy alloys and related concepts, Acta Mater. 122 (2017) 448-511, https://doi.org/10.1016/ j.actamat.2016.08.081.
- [14] E.P. George, D. Raabe, R.O. Ritchie, High-entropy alloys, Nat. Rev. Mater. 4 (2019) 515–534, https://doi.org/10.1038/s41578-019-0121-4.
- [15] B. Gludovatz, A. Hohenwarter, D. Catoor, E.H. Chang, E.P. George, R.O. Ritchie, A fracture-resistant high-entropy alloy for cryogenic applications, Science 345 (2014) 1153–1158, https://doi.org/10.1126/science.1254581.
- [16] Y.Q. Wang, B. Liu, K. Yan, M.S. Wang, S. Kabra, Y.L. Chiu, D. Dye, P.D. Lee, Y. Liu,

- B. Cai, Probing deformation mechanisms of a FeCoCrNi high-entropy alloy at 293 and 77 K using in situ neutron diffraction, Acta Mater. 154 (2018) 79–89, https://doi.org/10.1016/j.actamat.2018.05.013.
- [17] J.Y. He, W.H. Liu, H. Wang, Y. Wu, X.J. Liu, T.G. Nieh, Z.P. Lu, Effects of Al addition on structural evolution and tensile properties of the FeCoNiCrMn high-entropy alloy system, Acta Mater. 62 (2014) 105–113, https://doi.org/10.1016/j.actamat.2013.09.037.
- [18] R. Feng, M.C. Gao, C. Zhang, W. Guo, J.D. Poplawsky, F. Zhang, J.A. Hawk, J.C. Neuefeind, Y. Ren, P.K. Liaw, Phase stability and transformation in a light-weight high-entropy alloy, Acta Mater. 146 (2018) 280–293, https://doi.org/10.1016/j.actamat.2017.12.061.
- [19] X.Z. Gao, Y.P. Lu, B. Zhang, N.N. Liang, G.Z. Wu, G. Sha, J.Z. Liu, Y.H. Zhao, Microstructural origins of high strength and high ductility in an AlCoCrFeNi<sub>2.1</sub> eutectic high-entropy alloy, Acta Mater. 141 (2017) 59–66, https://doi.org/ 10.1016/j.actamat.2017.07.041.
- [20] Z.F. Lei, X.J. Liu, Y. Wu, H. Wang, S.H. Jiang, S.D. Wang, X.D. Hui, Y.D. Wu, B. Gault, P. Kontis, D. Raabe, L. Gu, Q.H. Zhang, H.W. Chen, H.T. Wang, J.B. Liu, K. An, Q.S. Zeng, T.G. Nieh, Z.P. Lu, Enhanced strength and ductility in a high-entropy alloy via ordered oxygen complexes, Nature 563 (2018) 546–550, https://doi.org/10.1038/s41586-018-0685-v.
- [21] Y.D. Wu, Y.H. Cai, Y.D. Wang, T. Wang, J.J. Si, J. Zhu, X.D. Hui, A refractory Hf<sub>25</sub>Nb<sub>25</sub>Ti<sub>25</sub>Zr<sub>25</sub> high-entropy alloy with excellent structural stability and tensile properties, Mater. Lett. 130 (2014) 277–280, https://doi.org/10.1016/ i.matlet.2014.05.134
- [22] V.T. Nguyen, M. Qian, Z. Shi, T. Song, L. Huang, J. Zou, A novel quaternary equiatomic Ti-Zr-Nb-Ta medium entropy alloy (MEA), Intermetallics 101 (2018) 39–43, https://doi.org/10.1016/j.intermet.2018.07.008.
- [23] N.N. Guo, L. Wang, L.S. Luo, X.Z. Li, Y.Q. Su, J.J. Guo, H.Z. Fu, Microstructure and mechanical properties of refractory MoNbHfZrTi high-entropy alloy, Mater. Des. 81 (2015) 87–94, https://doi.org/10.1016/j.matdes.2015.05.019.
- [24] M. Todai, T. Nagase, T. Hori, A. Matsugaki, A. Sekita, T. Nakano, Novel TiNb-TaZrMo high-entropy alloys for metallic biomaterials, Scripta Mater. 129 (2017) 65–68, https://doi.org/10.1016/j.scriptamat.2016.10.028.
- [25] S.P. Wang, J. Xu, TiZrNbTaMo high-entropy alloy designed for orthopedic implants: as-cast microstructure and mechanical properties, Mater. Sci. Eng. C 73 (2017) 80–89, https://doi.org/10.1016/j.msec.2016.12.057.
- [26] Y. Yuan, Y. Wu, Z. Yang, X. Liang, Z.F. Lei, H.L. Huang, H. Wang, X.J. Liu, K. An, W. Wu, Z.P. Lu, Formation, structure and properties of biocompatible TiZrHfNbTa high-entropy alloys, Mater. Res. Lett. 7 (2019) 225–231, https://doi.org/10.1080/21663831.2019.1584592.
- [27] O.N. Senkov, J.M. Scott, S.V. Senkova, D.B. Miracle, C.F. Woodward, Microstructure and room temperature properties of a high-entropy TaNbHfZrTi alloy, J. Alloys Compd. 509 (2011) 6043–6048, https://doi.org/10.1016/j.jallcom.2011.02.171.
- [28] C.C. Juan, M.H. Tsai, C.W. Tsai, C.M. Lin, W.R. Wang, C.C. Yang, S.K. Chen, S.J. Lin, J.W. Yeh, Enhanced mechanical properties of HfMoTaTiZr and HfMoNbTaTiZr refractory high-entropy alloys, Intermetallics 62 (2015) 76–83, https://doi.org/10.1016/j.intermet.2015.03.013.
- [29] W.Y. Ching, S. San, J. Brechtl, R. Sakidja, M. Zhang, P.K. Liaw, Fundamental electronic structure and multiatomic bonding in 13 biocompatible highentropy alloys, NPJ Comput. Mater. 6 (2020) 45, https://doi.org/10.1038/ s41524-020-0321-x.
- [30] N. Tüten, D. Canadinc, A. Motallebzadeh, B. Bal, Microstructure and tribological properties of TiTaHfNbZr high entropy alloy coatings deposited on Ti-6Al-4V substrates, Intermetallics 105 (2019) 99–106, https://doi.org/10.1016/j.intermet.2018.11.015.
- [31] Y.X. Ye, C.Z. Liu, H. Wang, T.G. Nieh, Friction and wear behavior of a single-phase equiatomic TiZrHfNb high-entropy alloy studied using a nanoscratch technique, Acta Mater. 147 (2018) 78–89, https://doi.org/10.1016/j.actamat.2018.01.014.
- [32] C. Mathiou, A. Poulia, E. Georgatis, A.E. Karantzalis, Microstructural features and dry - sliding wear response of MoTaNbZrTi high entropy alloy, Mater. Chem. Phys. 210 (2018) 126–135, https://doi.org/10.1016/ j.matchemphys.2017.08.036.
- [33] Y.Z. Shi, B. Yang, P.K. Liaw, Corrosion-resistant high-entropy alloys: a review, Metals 7 (2017) 43, https://doi.org/10.3390/met7020043.
- [34] A. Yamamoto, R. Honma, M. Sumita, Cytotoxicity evaluation of 43 metal salts using murine fibroblasts and osteoblastic cells, J. Biomed. Mater. Res. 39 (1998) 331–340, https://doi.org/10.1002/(sici)1097-4636, 199802)39: 2<331::aid-jbm22>3.0.co;2-e.
- [35] Q. Zhou, S. Sheikh, P. Ou, D. Chen, Q. Hu, S. Guo, Corrosion behavior of Hf<sub>0.5</sub>Nb<sub>0.5</sub>Ta<sub>0.5</sub>Ti<sub>1.5</sub>Zr refractory high-entropy in aqueous chloride solutions, Electrochem. Commun. 98 (2019) 63–68, https://doi.org/10.1016/ i.elecom.2018.11.009.
- [36] A. Chiba, K. Kumagai, N. Nomura, S. Miyakawa, Pin-on-disk wear behavior in a like-on-like configuration in a biological environment of high carbon cast and low carbon forged Co-29Cr-6Mo alloys, Acta Mater. 55 (2007) 1309—1318, https://doi.org/10.1016/j.actamat.2006.10.005.
- [37] N. Diomidis, S. Mischler, N.S. More, Manish Roy, Tribo-electrochemical characterization of metallic biomaterials for total joint replacement, Acta Biomater. 8 (2012) 852–859, https://doi.org/10.1016/j.actbio.2011.09.034.
- [38] Y. Yan, A. Neville, D. Dowson, Tribo-corrosion properties of cobalt-based medical implant alloys in simulated biological environments, Wear 263 (2007) 1105–1111, https://doi.org/10.1016/j.wear.2007.01.114.
- [39] Z. Doni, A.C. Alves, F. Toptan, J.R. Gomes, A. Ramalho, M. Buciumeanu,

- L. Palaghian, F.S. Silva, Dry sliding and tribocorrosion behaviour of hot pressed CoCrMo biomedical alloy as compared with the cast CoCrMo and Ti6Al4V alloys, Mater. Des. 52 (2013) 47–57, https://doi.org/10.1016/j.matdes.2013.05.032.
- [40] I. Cvijovic-Alagic, Z. Cvijovic, S. Mitrovic, V. Panic, M. Rakin, Wear and corrosion behaviour of Ti-13Nb-13Zr and Ti-6Al-4V alloys in simulated physiological solution, Corrosion Sci. 53 (2011) 796–808, https://doi.org/ 10.1016/j.corsci.2010.11.014.
- [41] P.A. Dearnley, B. Mallia, The chemical wear (corrosion-wear) of novel Cr based hard coated 316L austenitic stainless steels in aqueous saline solution, Wear 306 (2013) 263–275. https://doi.org/10.1016/i.wear.2012.09.002.
- [42] G. He, J. Eckert, W. Löser, M. Hagiwara, Composition dependence of the microstructure and the mechanical properties of nano/ultrafine-structured Ti-Cu-Ni-Sn-Nb alloys, Acta Mater. 52 (2004) 3035–3046, https://doi.org/ 10.1016/j.actamat.2004.03.006.
- [43] G. He, M. Hagiwara, Bimodal structured Ti-base alloy with large elasticity and low Young's modulus, Mater. Sci. Eng. C 25 (2005) 290–295, https://doi.org/ 10.1016/j.msec.2005.03.001.
- [44] B.B. Sun, M.L. Sui, Y.M. Wang, G. He, J. Eckert, E. Ma, Ultrafine composite microstructure in a bulk Ti alloy for high strength, strain hardening and tensile ductility, Acta Mater. 54 (2006) 1349–1357, https://doi.org/10.1016/ j.actamat.2005.11.011.
- [45] N.B. Hua, X.S. Hong, L.Y. Lin, Z.L. Liao, L. Zhang, X.Y. Ye, Q.T. Wang, Mechanical, corrosion, and wear performances of a biocompatible Ti-based glassy alloy, J. Non-Cryst. Solids 543 (2020) 120116, https://doi.org/10.1016/j.jnoncrysol.2020.120116.
- [46] Y. Liu, S.J. Pang, W. Yang, N.B. Huad, P.K. Liaw, T. Zhang, Tribological behaviors of a Ni-free Ti-based bulk metallic glass in air and a simulated physiological environment, J. Alloys Compd. 766 (2018) 1030–1036, https://doi.org/ 10.1016/j.jallcom.2018.07.023.
- [47] N.B. Hua, W.Z. Chen, Q.T. Wang, Q.H. Guo, Y.T. Huang, T. Zhang, Tribocorrosion behaviors of a biodegradable Mg<sub>65</sub>Zn<sub>30</sub>Ca<sub>5</sub> bulk metallic glass for potential biomedical implant applications, J. Alloys Compd. 745 (2018) 111–120, https://doi.org/10.1016/j.jallcom.2018.02.138.
- [48] N.B. Hua, Z.L. Liao, W.Z. Chen, Y.T. Huang, T. Zhang, Effects of noble elements on the glass-forming ability, mechanical property, electrochemical behavior and tribocorrosion resistance of Ni- and Cu-free Zr-Al-Co bulk metallic glass, J. Alloy, Compd 725 (2017) 403–414, https://doi.org/10.1016/j.jallcom.2017. 07.167.
- [49] W. Yang, Y. Liu, S.J. Pang, P.K. Liaw, T. Zhang, Bio-corrosion behavior and in vitro biocompatibility of equimolar TiZrHfNbTa high-entropy alloy, Intermetallics 124 (2020) 106845, https://doi.org/10.1016/j.intermet.2020. 106845.
- [50] S. Yadav, A. Kumar, K. Biswas, Wear behavior of high entropy alloys containing soft dispersoids (Pb, Bi), Mater. Chem. Phys. 210 (2018) 222–232, https://doi.org/10.1016/j.matchemphys.2017.06.020.
- [51] Y.X. Wang, Y.J. Yang, H.J. Yang, M. Zhang, S.G. Ma, J.W. Qiao, Microstructure and wear properties of nitrided AlCoCrFeNi high-entropy alloy, Mater. Chem. Phys. 210 (2018) 233–239, https://doi.org/10.1016/j.matchemphys.2017. 05.029
- [52] A. Ayyagari, C. Barthelemy, B. Gwalani, R. Banerjee, T.W. Scharf, S. Mukherjee, Reciprocating sliding wear behavior of high entropy alloys in dry and marine environments, Mater. Chem. Phys. 210 (2018) 162–169, https://doi.org/ 10.1016/j.matchemphys.2017.07.031.
- [53] J.F. Archard, Contact and rubbing of flat surfaces, J. Appl. Phys. 24 (1953) 981–988, https://doi.org/10.1063/1.1721448.
- [54] E. Hornbogen, The role of fracture toughness in the wear of metals, Wear 33 (1975) 251–259, https://doi.org/10.1016/0043-1648(75)90280-X.
- [55] Z.L. Liao, N.B. Hua, W.Z. Chen, Y.T. Huang, T. Zhang, Correlations between the wear resistance and properties of bulk metallic glasses, Intermetallics 93 (2018) 290–298, https://doi.org/10.1016/j.intermet.2017.10.008.
- [56] X. Yang, C.R. Hutchinson, Corrosion-wear of β-Ti alloy TMZF (Ti-12Mo-6Zr-2Fe) in simulated body fluid, Acta Biomater. 42 (2016) 429–439, https://doi.org/10.1016/j.actbio.2016.07.008.
- [57] N.B. Hua, X.S. Hong, Z.L. Liao, L. Zhang, X.Y. Ye, Q.T. Wang, P.K. Liaw, Corrosive wear behaviors and mechanisms of a biocompatible Fe-based bulk metallic glass, J. Non-Cryst. Solids 542 (2020), https://doi.org/10.1016/j.jnoncrysol.2020.120088, 120088.
- [58] M.T. Mathew, J.J. Jacobs, M.A. Wimmer, Wear-corrosion synergism in a CoCrMo hip bearing alloy is influenced by proteins, Clin. Orthop. Relat. Res. 470 (2012) 3109–3117, https://doi.org/10.1007/s11999-012-2563-5.
- [59] K. Komotori, N. Hisamori, Y. Ohmori, The corrosion/wear mechanisms of Ti-6Al-4V alloy for different scratching rates, Wear 263 (2007) 412–418, https://doi.org/10.1016/j.wear.2006.11.025.
- [60] J. Pellier, J. Geringer, B. Forest, Fretting-corrosion between 316L SS and PMMA: influence of ionic strength, protein and electrochemical conditions on material wear. Application to orthopaedic implants, Wear 271 (2011) 1563–1571, https://doi.org/10.1016/j.wear.2011.01.082.
- [61] D. Sun, J.A. Wharton, R.J.K. Wood, L. Ma, W.M. Rainforth, Microabrasion-corrosion of cast CoCrMo alloy in simulated body fluids, Tribol. Int. 42 (2009) 99–110, https://doi.org/10.1016/j.triboint.2008.05.005.
- [62] A. Motallebzadeh, N.S. Peighambardoust, S. Sheikh, H. Murakami, S. Guo, D. Canadin, Microstructural, mechanical and electrochemical characterization of TiZrTaHfNb and Ti<sub>1.5</sub>ZrTa<sub>0.5</sub>Hf<sub>0.5</sub>Nb<sub>0.5</sub> refractory high-entropy alloys for biomedical applications, Intermetallics 113 (2019) 106572, https://doi.org/

- 10.1016/j.intermet.2019.106572.
- [63] I. Milošev, G. Žerjav, J.M.C. Moreno, M. Popa, Electrochemical properties, chemical composition and thickness of passive film formed on novel Ti-20Nb-10Zr-5Ta alloy, Electrochim. Acta 99 (2013) 176-189, https://doi.org/10.1016/j.electacta.2013.03.086.
- [64] C. Vasilescu, S.I. Drob, J.M.C. Moreno, P. Osiceanu, M. Popa, E. Vasilescu, M. Marcu, P. Drob, Long-term corrosion resistance of new Ti-Ta-Zr alloy in simulated physiological fluids by electrochemical and surface analysis methods, Corrosion Sci. 93 (2015) 310-323, https://doi.org/10.1016/j.corsci.2015.01.038.